Improving the kinetic couplings in lattice nonrelativistic QCD

Christine T. H. Davies,[1,*] Judd Harrison,[1,2,†] Ciaran Hughes,[3,2,‡] Ronald R. Horgan,[2] Georg M. von Hippel,[4] and Matthew Wingate[2]

(HPQCD Collaboration)[§]

[1]*SUPA, School of Physics and Astronomy, University of Glasgow, Glasgow G12 8QQ, United Kingdom*
[2]*Department of Applied Mathematics and Theoretical Physics, University of Cambridge, Cambridge CB3 0WA, United Kingdom*
[3]*Fermi National Accelerator Laboratory, Batavia, Illinois 60510, USA*
[4]*Institut für Kernphysik, University of Mainz, Becherweg 45, 55099 Mainz, Germany*

(Received 1 January 2019; published 18 March 2019)

We improve the nonrelativistic QCD (NRQCD) action by comparing the dispersion relation to that of the continuum through $\mathcal{O}(p^6)$ in perturbation theory. The one-loop matching coefficients of the $\mathcal{O}(p^4)$ kinetic operators are determined, as well as the scale at which to evaluate α_s in the V-scheme for each quantity. We utilize automated lattice perturbation theory using twisted boundary conditions as an infrared regulator. The one-loop radiative corrections to the mass renormalization, zero-point energy and overall energy-shift of an NRQCD b-quark are also found. We also explore how a Fat3-smeared NRQCD action and changes of the stability parameter n affect the coefficients. Finally, we use gluon field ensembles at multiple lattice spacing values, all of which include u, d, s and c quark vacuum polarization, to test how the improvements affect the nonperturbatively determined $\Upsilon(1S)$ and $\eta_b(1S)$ kinetic masses, and the tuning of the b quark mass.

DOI: 10.1103/PhysRevD.99.054502

I. INTRODUCTION

The Standard Model (SM) of particle physics has been incredibly successful at describing experimental data to date [1,2]. However, in many ways, this success has been a double-edged sword; while SM predictions have overwhelmingly agreed with experimental measurements within errors, this has left little room for large new-physics effects to be observed. Consequently, to illuminate any new-physics phenomena high-precision tests of the SM must be performed. In the b-quark sector, the LHCb and BELLE II experiments will generate increasingly precise measurements. In response to this, we make the next level of improvement to the HPQCD Collaboration's formulation of the NRQCD action [3] which has been used for a number of state-of-the-art b-physics calculations [4–11].

In this study we will include, for the first time, operators in the NRQCD action which reproduce the correct quark dispersion relation to $\mathcal{O}(p^6)$. Then, with different values of the NRQCD stability parameter n, we use lattice perturbation theory to compute the kinetic matching coefficients to $\mathcal{O}(\alpha_s p^4)$. We remove the unphysical tadpole contributions [12] from the lattice action and give perturbative results for two different tadpole improvement programs: the first by using a mean-field improvement parameter in Landau gauge u_0 [12], and the second via Fat3 smearing [13]. Additionally, we determine the one-loop (bare-to-pole) mass renormalization and zero-point energy of the b-quark. These can be combined to give the one-loop energy shift of the NRQCD heavy quark and added to nonperturbatively obtained static masses to give numerical results which, after converting from lattice units to GeV, can be compared to experimental data. Further, for each of these quantities the scale $\mu = q^*$ at which to evaluate the strong coupling constant defined in the V-scheme is determined using the Brodsky-Lepage-Mackenzie (BLM) procedure [12,14].

After perturbatively determining the full one-loop radiative corrections to the kinetic couplings, we nonperturbatively determine the $\Upsilon(1S)$ and $\eta_b(1S)$ energies in order to examine how improving the NRQCD action, both with additional $\mathcal{O}(p^6)$ operators and with the $\mathcal{O}(\alpha_s p^4)$ couplings, reduces the effect of lattice artifacts.

*christine.davies@glasgow.ac.uk
†Judd.Harrison@glasgow.ac.uk
‡chughes@fnal.gov
§http://www.physics.gla.ac.uk/HPQCD

This paper is organized as follows. In Sec. II we describe the improved NRQCD action. In Sec. III we match the $\mathcal{O}(\alpha_s p^4, p^6)$ NRQCD dispersion relation to the continuum, describe our tadpole improvement procedures and how the scale at which to evaluate α_V is found. Section III A describes the computational setup of the automated lattice perturbation theory, while Sec. III B gives an analysis of the perturbative results. Section IV gives details of the nonperturbative calculation and Sec. IV B presents the nonperturbative results. We summarize our findings in Sec. V.

II. *b*-QUARKS USING NRQCD

Information about processes involving heavy quarks can be computed on the lattice using correlation functions constructed from combinations of heavy-quark propagators. Current lattice ensembles have small enough lattice spacings and large enough volumes so that accurate relativistic *c*-quark formalisms (e.g., highly improved staggered quarks (HISQ) [15]) are available. Since the *b*-quark has a Compton wavelength of $\mathcal{O}(0.04)$ fm, most current lattice ensembles cannot resolve relativistic *b*-quarks since $am_b > 1$ [16].[1] However, it is well known that *b*-quarks are very nonrelativistic inside their bound states (with $v_{\mathrm{rel}}^2 \approx 0.1$ for low-lying bottomonium states) and thus using a nonrelativistic effective field theory, which has a formal expansion in $p/m_b = v_{\mathrm{rel}}$ [18], is very appropriate. This effective field theory is then discretized as lattice NRQCD [18].

HPQCD's formulation of lattice NRQCD has already proven successful in producing accurate *b*-physics results in the literature. For example, the NRQCD formalism that gave a quark dispersion relation correct to $\mathcal{O}(\alpha_s p^4)$ has already been used to study bottomonium *S*, *P* and *D* wave mass splittings [3,4], *B* meson mass splittings [5], *B* meson decay constants [6,19], Υ and Υ' leptonic widths [7]. Subsequently, the spin-dependent $\mathcal{O}(v^6)$ operators were added to that NRQCD action in order to compute hindered M1 radiative decays [8], precise bottomonium hyperfine splittings [9,10][2] and to aid in the search for $bb\bar{b}\bar{b}$-type bound tetraquarks [11].

Given the increasingly important emphasis being put on high-precision calculations needed to keep pace with measurements from the LHCb and BELLE II experiments, we take the next steps in improving the lattice NRQCD action to reduce the systematic uncertainties in future theoretical calculations using it. The first part of this improvement is to add the necessary operators to the aforementioned NRQCD action that reproduce the correct $\mathcal{O}(p^6)$ quark dispersion relation at tree level.

[1]Combining results at multiple lattice spacing values and multiple heavy quark masses with a highly improved relativistic action does allow results to be obtained at the physical *b* quark mass [17].

[2]Four-quark operators were also used in this study.

The NRQCD action that gives rise to a $\mathcal{O}(p^6)$ correct quark dispersion relation, including $\mathcal{O}(v^4)$ interaction operators [3], produces a heavy-quark propagator which can be found through the evolution equation

$$\begin{aligned} G(\mathbf{x}, t+1) &= e^{-aH} G(\mathbf{x}, t), \\ G(\mathbf{x}, t_{\mathrm{src}}) &= \phi(\mathbf{x}), \end{aligned} \tag{1}$$

where $\phi(x)$ is a source function and

$$\begin{aligned} e^{-aH} &= \left(1 - \frac{a\delta H|_{t+1}}{2}\right)\left(1 - \frac{aH_0|_{t+1}}{2n}\right)^n U_t^\dagger(x) \\ &\quad \times \left(1 - \frac{aH_0|_t}{2n}\right)^n \left(1 - \frac{a\delta H|_t}{2}\right), \\ aH_0 &= -\frac{\Delta^{(2)}}{2am_b}, \\ a\delta H &= a\delta H_{v^4} + a\delta H_{p^6}; \end{aligned} \tag{2}$$

$$\begin{aligned} a\delta H_{v^4} &= -c_1 \frac{(\Delta^{(2)})^2}{8(am_b)^3} + c_2 \frac{i}{8(am_b)^2}(\boldsymbol{\nabla}\cdot\tilde{\mathbf{E}} - \tilde{\mathbf{E}}\cdot\boldsymbol{\nabla}) \\ &\quad - c_3 \frac{1}{8(am_b)^2}\boldsymbol{\sigma}\cdot(\tilde{\boldsymbol{\nabla}}\times\tilde{\mathbf{E}} - \tilde{\mathbf{E}}\times\tilde{\boldsymbol{\nabla}}) \\ &\quad - c_4 \frac{1}{2am_b}\boldsymbol{\sigma}\cdot\tilde{\mathbf{B}} + c_5 \frac{\Delta^{(4)}}{24am_b} - c_6 \frac{(\Delta^{(2)})^2}{16n(am_b)^2}, \\ \delta H_{p^6} &= -\frac{c_{(p^2)^3}}{16(am_b)^5}\left(1 - \frac{(am_b)^2}{6n^2}\right)(\Delta^{(2)})^3 \\ &\quad - \frac{c_{p^6}}{180am_b}\Delta^{(6)} + \frac{c_{p^2p^4}}{48(am_b)^3}(\Delta^{(2)}\Delta^{(4)}). \end{aligned} \tag{3}$$

Here, am_b is the bare *b*-quark mass, ∇ is the symmetric lattice derivative, with $\tilde{\nabla}$ the improved version, and $\Delta^{(2)}$, $\Delta^{(4)}$, $\Delta^{(6)}$ are the lattice discretizations of $\sum_i D_i^2$, $\sum_i D_i^4$ and $\sum_i D_i^6$ respectively, with our conventions given in Appendix A. $\tilde{\mathbf{E}}$, $\tilde{\mathbf{B}}$ are the improved chromoelectric and chromomagnetic fields, details of which can be found in [3]. Each of these fields, as well as the covariant derivatives, must be tadpole-improved using the same improvement procedure as in the perturbative calculation of the matching coefficients [12]. This will be discussed further in Sec. II B. The parameter n is used to prevent instabilities at large momentum from the kinetic energy operator and needs to satisfy the constraint $p^2 < 4nam_b$. A choice of $n = 4$ was suitable for values of am_b used in previous nonperturbative studies. We choose to put the $a\delta H_{p^6}$ corrections into $a\delta H$ rather than alter aH_0 so that the kinetic operator remains unchanged. This formulation is also consistent with previous HPQCD NRQCD actions, is symmetric with respect to time reversal and has smaller renormalizations than other formulations [18]. The rotationally symmetry breaking operators (which vanish as $a \to 0$) with coefficients c_{p^6}

and $c_{p^2p^4}$ in δH_{p^6} remove higher-order discretization effects from using finite-difference derivatives. The operator with coefficient $c_{(p^2)^3}$ correctly adds the term proportional to $(\mathbf{p}^2)^3$ into the heavy-quark dispersion relation.

The matching coefficients c_i in the above Hamiltonian take into account the high-energy UV modes from QCD processes that are not present in NRQCD. Each c_i can be fixed by matching a particular lattice NRQCD formalism to full continuum QCD. Each c_i can be expanded perturbatively as

$$c_i = 1 + c_i^{(1)}\alpha_s + \mathcal{O}(\alpha_s^2), \tag{4}$$

and, after tadpole improvement [12], we expect $c_i^{(1)}$ to be $\mathcal{O}(1)$. In Sec. II A, we will match the on shell NRQCD dispersion relation to that of the continuum and determine $c_1^{(1)}$, $c_6^{(1)}$ and $c_5^{(1)}$. Each of these coefficients should exhibit benign behavior as a function of am_b in the regime where the NRQCD effective field theory is well-behaved. In contrast, the coefficient may diverge as the effective field theory breaks down as $p \sim \pi/a$ gets too large or am_b gets too small. We take tree level values, $c_i = 1$, for the coefficients appearing in δH_{p^6}.

We call the NRQCD Hamiltonian presented in Eq. (3) the $\mathcal{O}(p^6)$ Hamiltonian, while choosing $a\delta H_{p^6} = 0$ produces the $\mathcal{O}(p^4)$ Hamiltonian. When including the one-loop corrections to c_1, c_6 and c_5, we denote the $\mathcal{O}(p^6)$ NRQCD action as being $\mathcal{O}(\alpha_s p^4, p^6)$, while if $\delta H_{p^6} = 0$ then the action is $\mathcal{O}(\alpha_s p^4)$.

A. One-loop matching to $\mathcal{O}(\alpha_s p^4, p^6)$

A high-precision nonperturbative calculation of mass splittings will require knowledge of at least the $\mathcal{O}(\alpha_s)$ corrections to the matching coefficients in order to improve upon existing few percent errors. For example, when tuning the bare quark mass am_b fully nonperturbatively in NRQCD, one computes the kinetic mass of a hadron[3] [3]. This kinetic mass depends on the internal kinematics of the hadron, and hence on (at least) the terms c_1, c_5, and c_6 in the Hamiltonian. These matching coefficients are known as the kinetic couplings [20].

The kinetic couplings can be found perturbatively by matching the NRQCD on shell energy (which corresponds to the location of the pole of the quark propagator in the interacting theory) to the continuum QCD dispersion relation. From now on, to avoid superfluous notation, we will implicitly work in lattice units unless otherwise stated. To $\mathcal{O}(\alpha_s)$ the inverse quark propagator may be written in momentum space as

$$G(p)^{-1} = G^{(0)}(p)^{-1} - \alpha_s \Sigma(p), \tag{5}$$

with $G^{(0)}(p)^{-1}$ the quark propagator obtained at tree-level from the noninteracting part of the NRQCD action, $\Sigma(p)$ the one-loop quark self-energy, $p = (p_4, \mathbf{p})$ a four-vector in Euclidean space and $\omega = -ip_4$ the energy in Minkowski space. The free quark propagator can be explicitly found as

$$G^{(0)}(p)^{-1} = \{1 - e^{-ip_4} F(p)^{2n} F_1(p)^2\}, \tag{6}$$

$$F(p) = 1 - \frac{1}{nm_b}\sum_j \sin^2(p_j/2), \tag{7}$$

$$\begin{aligned} F_1(p) = 1 &- \frac{c_5}{3m_b}\sum_j \sin^4(p_j/2) \\ &+ \frac{\tilde{c}_1}{m_b^3}\left[1 + \frac{m_b}{2n}\right]\left[\sum_j \sin^2(p_j/2)\right]^2 \\ &- \frac{2c_{(p^2)^3}}{m_b^5}\left[1 - \frac{m_b^2}{6n^2}\right]\left[\sum_j \sin^2(p_j/2)\right]^3 \\ &- \frac{8c_{p^6}}{45m_b}\sum_j \sin^6(p_j/2) \\ &+ \frac{2c_{p^2p^4}}{3m_b^3}\sum_{j,k} \sin^2(p_j/2)\sin^4(p_k/2), \end{aligned} \tag{8}$$

where we have defined $\tilde{c}_1 = (c_1 + c_6 m_b/2n)/(1 + m_b/2n)$ for computational ease, and $c_1 = c_6 = \tilde{c}_1$. The term $F(p)$ arises from the noninteracting momentum space part of $(1 - H_0/2n)$ in (2), while $F_1(p)$ comes from the $(1 - \delta H/2)$ piece.

To find the NRQCD dispersion relation we determine the on shell energy $\omega(\mathbf{p})$ which causes a pole in the full heavy-quark propagator. The one-loop $\omega(\mathbf{p})$ can be found from Eqs. (5) and (6) as

$$\omega(\mathbf{p}) = -\log\left(F^{2n}(\mathbf{p})F_1^2(\mathbf{p})\right) - \alpha_s \Sigma(\omega_0(\mathbf{p}), \mathbf{p}) \tag{9}$$

with $\omega_0(\mathbf{p}) = -\log(F^{2n}(\mathbf{p})F_1^2(\mathbf{p}))$, with tree-level coefficients in F and F_1, being the tree-level on shell energy found by setting the tree-level inverse propagator in Eq. (6) to zero. We have constructed the Hamiltonian in Eq. (2) to produce a nonrelativistic dispersion relation correct to $\mathcal{O}(p^6)$, and we now include the $\mathcal{O}(\alpha_s p^4)$ correction. This yields[4]

$$\begin{aligned} \omega_0(\mathbf{p}) = &\frac{\mathbf{p}^2}{2m_b} - \frac{(\mathbf{p}^2)^2}{8m_b^3} + \frac{(\mathbf{p}^2)^3}{16m_b^5} \\ &+ \alpha_s\left\{c_5^{(1)}\frac{\mathbf{p}^4}{24m_b} - \tilde{c}_1^{(1)}\left(\frac{1}{m_b} + \frac{1}{2n}\right)\frac{(\mathbf{p}^2)^2}{8m_b^2}\right\}. \end{aligned} \tag{10}$$

[3]The static mass (the energy corresponding to zero-spatial momentum) in lattice NRQCD [3] is shifted due to the removal of the mass term from the Hamiltonian, and so one can only tune static mass differences fully nonperturbatively.

[4]We correct a typographical error in Appendix B of [3].

When matching the dispersion relation to $\mathcal{O}(\alpha_s p^4, p^6)$, it is necessary to decompose the self-energy $\Sigma(p)$ using the small-$\mathbf{p}$ expansion [20] as

$$\Sigma(p) = \Sigma_0(\omega) + \Sigma_1(\omega)\frac{\mathbf{p}^2}{2m_b} + \Sigma_2(\omega)\frac{(\mathbf{p}^2)^2}{8m_b^2} + \Sigma_3(\omega)\mathbf{p}^4. \tag{11}$$

Further, when ω is small, each function has a well-defined series expansion $\Sigma_m(\omega) = \sum_{l=0}^{\infty}\Sigma_m^{(l)}\omega^l$. The $\Sigma_m^{(l)}$ can be found from derivatives of the quark self-energy as

$$\Sigma_0(\omega) = \Sigma(\mathbf{p} = \mathbf{0}), \tag{12}$$

$$\Sigma_1(\omega) = m_b\frac{\partial^2\Sigma(p)}{\partial p_z^2}\bigg|_{\mathbf{p}=\mathbf{0}}, \tag{13}$$

$$\Sigma_2(\omega) = m_b^2\frac{\partial^4\Sigma(p)}{\partial p_z^2\partial p_y^2}\bigg|_{\mathbf{p}=\mathbf{0}}, \tag{14}$$

$$\Sigma_3(\omega) = \frac{1}{24}\left(\frac{\partial^4\Sigma(p)}{\partial p_z^4} - 3\frac{\partial^4\Sigma(p)}{\partial p_z^2\partial p_y^2}\right)\bigg|_{\mathbf{p}=\mathbf{0}}, \tag{15}$$

$$\Sigma_m^{(l)} = (-i)^l\frac{1}{l!}\frac{\partial^l\Sigma_m(p_4)}{\partial p_4^l}\bigg|_{p_4=0}. \tag{16}$$

Then, by using the tree-level ω_0 from (10) in Eq. (11) we find

$$\Sigma(\omega_0, \mathbf{p}) = W_0 + \frac{\mathbf{p}^2}{2m_b}Z_m^{(1)} + \frac{(\mathbf{p}^2)^2}{8m_b^2}\left\{W_1 - \frac{3Z_m^{(1)}}{m_b}\right\} + W_2\mathbf{p}^4, \tag{17}$$

$$m_b^r = Z_m m_b = m_b(1 + \alpha_s Z_m^{(1)} + \mathcal{O}(\alpha_s^2)), \tag{18}$$

$$Z_m^{(1)} = \Sigma_0^{(1)} + \Sigma_1^{(0)}, \tag{19}$$

$$W_0 = \Sigma_0^{(0)}, \tag{20}$$

$$W_1 = 2\Sigma_0^{(2)} + 2\Sigma_1^{(1)} + \Sigma_2^{(0)} + \frac{2\Sigma_0^{(1)}}{m_b} + \frac{3\Sigma_1^{(0)}}{m_b}, \tag{21}$$

$$W_2 = \Sigma_3^{(0)}, \tag{22}$$

where the superscript "r" denotes renormalized quantities and $Z_m^{(1)}$ is the $\mathcal{O}(\alpha_s)$ coefficient of the bare-to-pole mass renormalization. Substituting (8) and (17) into (9) gives the one-loop NRQCD dispersion relation to $\mathcal{O}(\alpha_s p^4, p^6)$ as

$$\omega(\mathbf{p}) = \frac{\mathbf{p}^2}{2m_b^r} - \frac{(\mathbf{p}^2)^2}{8(m_b^r)^3} + \frac{(\mathbf{p}^2)^3}{16(m_b^r)^5} - \alpha_s\{W_0 + \mathbf{p}^4\left[W_2 - \frac{c_5^{(1)}}{24m_b}\right] + \frac{(\mathbf{p}^2)^2}{8m_b^2}\left[\left(\frac{1}{m_b} + \frac{1}{2n}\right)\tilde{c}_1^{(1)} + W_1\right]\}. \tag{23}$$

Matching Eq. (23) to the continuum QCD dispersion relation [3,21] gives the matching coefficients for $\tilde{c}_1^{(1)}, c_5^{(1)}$ as well as the energy shift of a heavy quark (to this order) as

$$\tilde{c}_1^{(1)} = -\left(\frac{1}{m_b} + \frac{1}{2n}\right)^{-1}W_1, \tag{24}$$

$$c_5^{(1)} = 24m_b W_2, \tag{25}$$

$$C = \omega^{(\mathrm{QCD})} - \omega = m_b^r + \alpha_s W_0 = m_b(1 + \alpha_s\delta C), \tag{26}$$

$$\delta C = Z_m^{(1)} + \frac{W_0}{m_b}. \tag{27}$$

The shift C is the perturbative shift of the zero of energy. For each heavy quark in a nonperturbative calculation, the shift can be added to the simulation energy and, after being converted from lattice units to GeV, this can then be compared to experimental masses [20,21]. In practice hadron masses can be more precisely determined fully nonperturbatively through their kinetic mass in lattice QCD.

The aim of this study is to determine the one-loop coefficients $\tilde{c}_1^{(1)}$, $c_5^{(1)}$, δC (and thus also $Z_m^{(1)}$ and W_0) for different improved NRQCD actions to find the best way forward for increasingly accurate nonperturbative calculations in the future. Before these coefficients can be used, it is first necessary to remove unphysical contributions from tadpole diagrams which can cause the coefficients to be rather large [12].

B. Tadpole improvement

The authors of Ref. [12] show that using Lie group elements when constructing the lattice field theory introduces unphysical tadpole diagrams which do not contribute to continuum schemes. These unphysical tadpole diagrams cause large, process independent renormalizations and produce a poor convergence of the perturbative series. Reference [12] also suggests a solution to this: a gauge-invariant mean-field improvement program (tadpole-improvement) where each lattice link, $U_\mu(x)$, is scaled to $U_\mu(x)/u_0$. We choose u_0 to be the mean link in Landau gauge, i.e., $u_0 = \langle\frac{1}{3}\mathrm{Tr}U_\mu(x)\rangle$. This mean-field parameter has been calculated for the Symanzik-improved gluon

[3,22] action both perturbatively to one-loop (with $u_0 = 1 - \alpha_s u_0^{(2)}$ giving $u_0^{(2)} = 0.750$) [23] and nonperturbatively [3,6] (where the value of u_0 depends on the ensemble used, e.g., see Table IV). After a tadpole improvement procedure has been implemented, the one-loop coefficients are expected to be $\mathcal{O}(1)$. The same tadpole-improvement program must of course be implemented in the nonperturbative calculations as has been used for the perturbative calculations.

Before the mean-field improvement procedure is performed, care must be taken to ensure that any link-pair cancellations $U_\mu^\dagger(x)U_\mu(x) = 1$ occur in the lattice action used in both nonperturbative and perturbative calculations. Such cancellations do not generate any unphysical tadpole diagrams and scaling by $1/u_0^2$ would be incorrect. Yet, expanding out the complicated NRQCD Hamiltonian in (2) in terms of links $U_\mu(x)$ is excessively expensive for numerical calculations. Consequently, link-pair cancellations are only taken into account separately for each derivative, $(\Delta^{(2n)})^m$, or field strengths [$E_i(x)$ or $B_i(x)$] appearing in the action. This is called partial cancellation [3,21]. The difference between the complete and partial cancellation prescriptions was empirically shown not to be sizable [21]. Formulas for the partially cancelled derivatives are given in Appendix A.

By using the partially cancelled mean-field improvement procedure just described, one can find the $\mathcal{O}(\alpha_s)$ tadpole counterterms for the one-loop quantities described in Sec. II A. For the NRQCD action without the $\mathcal{O}(p^6)$ operators, the computation of the tadpole counterterms was checked in two separate calculations. The first was performed analytically, and the second using a MATHEMATICA script. Both calculations reproduced the results of [21] (in the case where the additional parameter used there, v, is set to zero) and [3,24]. We extended the numerical code to include the $\mathcal{O}(p^6)$ operators. The one-loop tadpole counterterms are given in Appendix B. After the (unimproved) one-loop quantities have been found in lattice perturbation theory, we can add the appropriate tadpole counterterms to determine the improved values. This will be discussed further in Sec. III B.

As can be seen in Appendix B, the mean-field counterterms obtained from using the $\mathcal{O}(p^6)$ NRQCD action contain higher-orders of $1/m_b$ relative to the counterterms obtained from using the $\mathcal{O}(p^4)$ NRQCD action. This is a consequence of partially cancelling the derivative operators $(\Delta^{(2n)})^m$, whose counterterms are given in Appendix A. The impact of this becomes pronounced as am_b is reduced as will become evident in Sec. III.

In this study, we choose to account for the unphysical tadpole contributions using two different prescriptions. The first prescription proceeds via the partially cancelled mean-field improvement procedure just described. The one-loop tadpole counterterms given in Appendix B, which depend on $1/am_b$, remove the unphysical tadpoles. As seen in Sec. III B, the improved values give smaller absolute renormalizations compared to the unimproved case and exhibit a longer plateau over a larger range in am_b indicating stable behavior in the effective field theory. However, the tadpole counterterms from using the $\mathcal{O}(p^6)$ action diverge faster as $am_b \to 0$ due to the higher-order terms in $1/am_b$, and therefore the tadpole-improved one-loop results obtained from the $\mathcal{O}(p^6)$ NRQCD action also diverge faster (see Sec. III B). This could be slightly inconvenient for ensembles with increasingly small lattice spacings, such as the superfine ensembles currently in use [25], which have a lattice spacing of $a \approx 0.06$ fm.

Because of this, we explore an alternative improvement procedure based on the fattening of gauge-links [13,26]. The fat7-smeared link [27] introduces staples of up to seven-link paths to completely remove the tree-level couplings to gluons with high transverse-momentum modes equal to $\pm\pi$. As the fat7 link is computationally expensive, alternative fat-links have been designed based on three- or five-link staples, called fat3 and fat5 respectively. These latter links reduce the couplings to gluons with high transverse-momentum and suppress unphysical tadpole diagrams [27]. This will be discussed further in Sec. III B. Therefore, we also explore, for the first time, how a fat3-smeared NRQCD action correct to $\mathcal{O}(p^4)$ affects the renormalization of kinetic couplings. Here the fattened links are projected back onto $U(3)$ [26] [not $SU(3)$].

The last piece of information needed to use the tadpole-improved one-loop coefficients in a nonperturbative computation is the scale, q^*, at which to evaluate the strong coupling constant.

C. Determining the scale of α_s

The Brodsky-Lepage-Mackenzie procedure [12,28] determines an optimal q^* for α_V, the coupling defined using the heavy quark potential [28], by examining the momentum flowing through a gluon in the one-loop Feynman diagram. In this prescription, one studies the one-loop integral of a fully dressed gluon within a particular diagram, then uses the running of $\alpha_V(q)$ to find a mean-value q^* which reproduces the integral. To do this, one expands the running of $\alpha_V(q)$ as a polynomial in $\log(q^2/q^{*2})$ and assumes that the leading order log-moments are the dominant contributions. However, in certain areas of parameter space, the leading order log-moments can be anomalously small and give unphysically large or small erroneous q^*. This was noticed in [20] after which [14] determined q^* when the zeroth and first log-moments are anomalously small via

$$\log(q^{*2}) = \langle\!\langle \log(q^2) \rangle\!\rangle \pm [-\sigma^2]^{\frac{1}{2}}, \tag{28}$$

where $\langle\!\langle \log(q^2) \rangle\!\rangle = \langle f(q)\log(q^2)\rangle / \langle f(q)\rangle$ indicates the weighted average, $f(q)$ is the integrand of the one-loop

Feynman diagram, and $\sigma^2 = \langle\!\langle \log^2(q^2) \rangle\!\rangle - \langle\!\langle \log(q^2) \rangle\!\rangle^2$. The appropriate choice of $\pm$ in Eq. (28) is usually clear based on requiring q^* to be continuous and physically sensible, although the ambiguity can be removed by calculating higher log-moments [14]. When $\sigma^2 > 0$, only the first term in Eq. (28) is used. However, when $\sigma^2 < 0$, Eq. (28) takes into account the anomalies to first order.

The unphysical tadpole diagrams contribute to the scale q^*, using the mean-field improvement prescription described in Sec. II B will alter its value. When the tadpole counterterm $c_{\rm tad}\alpha_V(q^*_{\rm tad})$ is added to the one-loop contribution $c_a\alpha_V(q^*_a)$, the second-order formula (28) is altered to [14]

$$\log(q^{*2}) = \frac{c_a \langle\!\langle \log(q^2) \rangle\!\rangle_a + c_{\rm tad} \langle\!\langle \log(q^2) \rangle\!\rangle_{\rm tad}}{c_a + c_{\rm tad}} \pm [-\sigma^2]^{\frac{1}{2}} \tag{29}$$

$$\sigma^2 = \frac{c_a \langle\!\langle \log^2(q^2) \rangle\!\rangle_a + c_{\rm tad} \langle\!\langle \log^2(q^2) \rangle\!\rangle_{\rm tad}}{c_a + c_{\rm tad}} - \left(\frac{c_a \langle\!\langle \log(q^2) \rangle\!\rangle_a + c_{\rm tad} \langle\!\langle \log(q^2) \rangle\!\rangle_{\rm tad}}{c_a + c_{\rm tad}} \right)^2 . \tag{30}$$

Again, if $\sigma^2 > 0$, then only the first-order term in Eq. (29) is needed and used, while if $\sigma^2 < 0$ both terms are needed to yield physical results.

Theoretically, we expect $a\Lambda_{\rm QCD} < aq^* < \pi$ as the one-loop corrections take into account UV modes neglected by imposing a momentum cutoff. Even though the corrected second order formula given in Eq. (29) was used, unphysical values of q^* for certain values of am_b in the one-loop quantities were sometimes obtained. In these cases, although rare, it was usually clear that the issue was due to the 0th–2nd log-moments being anomalously small. To rectify this issue, we use the simple nth-order formula given by [14]

$$\log(q^{*2}) = \frac{\langle f_a(q) \log^n(q^2) \rangle + \langle f_{\rm tad}(q) \log^n(q^2) \rangle}{n \langle f_a(q) \log^{n-1}(q^2) \rangle + n \langle f_{\rm tad}(q) \log^{n-1}(q^2) \rangle} . \tag{31}$$

Leaving the tadpole pieces out of Eq. (31) gives the higher-order tadpole-unimproved scale. As we do not mean-field improve the fat3-smeared one-loop quantities, the above formulas with the tadpole pieces set to zero are used to find q^* in the case of fat3-smeared links.

III. PERTURBATIVE DETERMINATION OF ONE-LOOP QUANTITIES

A. Perturbative computational details

Due to the complexity of the NRQCD action that we utilize, an efficient computational methodology is needed to calculate the Feynman integrals of the one-loop formulas given in (21) and (22). Fortunately, the theory behind the automatic generation of Feynman rules for complex lattice actions exists [26,29]. Here, we employ the automated lattice perturbation theory routines HiPPy and HPsrc [26,30]. These routines have been thoroughly tested and used in previous perturbative calculations [3,5,21,22,31]. Given that we will produce results for a number of different NRQCD actions, these automated packages are ideal.

We automatically generate the Feynman rules for a specific NRQCD action (along with the Symanzik-improved gluonic action [3,31]) using the HiPPy package. We can then construct the Feynman diagrams in a generic fashion using the HPsrc package, which will use these Feynman rules to numerically evaluate the diagram, along with its derivatives thanks to automated differentiation techniques [26,32].

In the matching procedure both the continuum and lattice contributions to the dispersion relation are separately infrared (IR) finite. However, intermediate steps on the lattice may produce IR divergences which cancel when evaluating the one-loop quantities. To regulate the IR divergences, we use twisted boundary conditions (TBCs) on a finite-volume lattice where the momentum integral is replaced by a summation over momentum modes [29]. TBCs introduce a lower momentum cutoff by removing the zero mode from the gluon propagator. Specifically, we employ triple-twist boundary conditions with an appropriate squashing factor in the untwisted temporal direction (used to broaden peaks of the integrand, thus removing most of the dependence on L [29]). Computational details of both concepts are described in [26,31], and we refer the reader to those articles for further details. All numerical results are IR finite as expected. As the dispersion relation is UV finite, this allows us to directly equate results obtained on the lattice to those obtained in the continuum. Furthermore, we test that the gauge-invariant quantities are independent of the gluon propagator gauge parameter by working in both Feynman gauge and Landau gauge. All perturbative results presented, except for the Landau-gauge mean-field parameter $u_0^{(2)}$, will be in Feynman gauge.

The one-loop contributions to the self-energy are shown in Fig. 1. Care must be taken when numerically evaluating the rainbow diagram so that the pole of the heavy-quark propagator does not cross the temporal integration contour. Details of our implementation of the contour shift can be found in [21].

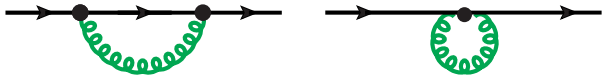

FIG. 1. Contributions to the one-loop self energy Σ of the heavy quark, showing the *rainbow* diagram (left) and the *tadpole* diagram (right). The straight lines represent heavy quarks, while the curly lines represent gluons.

In this study we will always take the spatial box length to be $4 \leq L \leq 16$ and choose a temporal extent of $T = 16L$. This allows the pole structure to be resolved in greater detail and reduces finite-T effects. As the one-loop integration is carried out by direct summation of the twisted momentum modes, numerical results are exact [31]. We follow the approach suggested by [33] in order to fit exact data. Here, our exact results from TBCs can be expressed as a polynomial in $1/L$ [29], yet we are only interested in knowing the constant term (corresponding to the infinite-volume result). We may use priors to model the polynomial dependence and then marginalize [34] from the exact data the part of the polynomial that we are not interested in. Using a finite-degree polynomial of order N to model the exact results, we find that $N = 20$ is a suitable choice and check that all results are unchanged with its variation. Marginalizing the last $N - N_L$ terms of this polynomial into the exact data and then performing a Bayesian fit [33,35] to a polynomial of degree N_L successfully determines the desired constant parameter of the polynomial. As is common with marginalized Bayesian fits [34], marginalizing all but one or two fit parameters produces stable and precise results and has seen wide success [8,36]. Even though we produce successful fits when marginalizing all but the constant term, we choose $N_L = 5$ and ensure that there is no sensitivity to this.

In the following section, we will give perturbative results for three NRQCD actions: (i) the $\mathcal{O}(p^6)$ NRQCD action with stability parameter $n = 4$ as described in Sec. II; (ii) the $\mathcal{O}(p^4)$ NRQCD action with stability parameter $n = 4$, 6 and 8; and (iii) a fat3-smeared $\mathcal{O}(p^4)$ NRQCD action with stability parameter $n = 4$ and no mean-field improvement. For a fixed quark and gauge action the one-loop coefficients depend only on the input parameter am_b. We calculate results for a range of am_b values, enabling interpolation to values not explicitly calculated that may be useful for lattice calculations. This also allows us to demonstrate the functional dependence on am_b graphically to see where the divergent behavior begins as am_b goes to zero.

B. Perturbative results and analysis

We calculate W_1 and W_2 for both the $\mathcal{O}(p^4)$ and $\mathcal{O}(p^6)$ actions with $n = 4$ (including all log moments) with spatial extent $L = 4$, 6, 8, 10, 16. We then successfully fit this data using the methodology described in Sec. III A. Figure 2 shows an example of this, with the raw W_1 data at multiple values of $1/L$ overlaid against the fit curve. In fact, we found Bayesian fitting to a polynomial so successful that we only needed data with $L = 4$, 6, 8, 10 to obtain the constant term to subpercent precision in general. Consequently, we calculate data for W_1 and W_2 for an $\mathcal{O}(p^4)$ action with $n = 6$, 8 and with $L = 4$, 6, 8, 10, as well as all $Z_m^{(1)}$, W_0 and fat3-smeared results (including log moments). The short computational time needed to calculate $u_0^{(2)}$ (and its log moments), meant that we were able to do this on lattices of size $L = 4$, 6, 8, 10, 12, 14, 16. We present the infinite-volume results for the mean-field unimproved W_1 and W_2 in Fig. 3. Also shown on each figure is a smooth interpolating curve between the results. This interpolating curve was chosen to be a polynomial in $1/am_b$ in order to reproduce the static limit as $m_b \to \infty$. It is expected that all one-loop quantities diverge as $am_b \to 0$

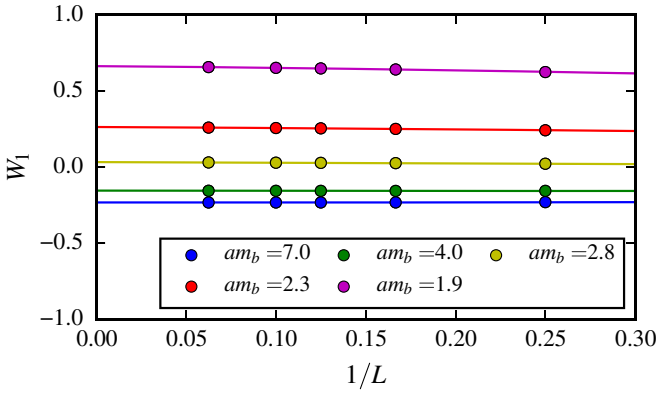

FIG. 2. The raw data for W_1 at multiple values of $1/L$ overlaid with our fit curve.

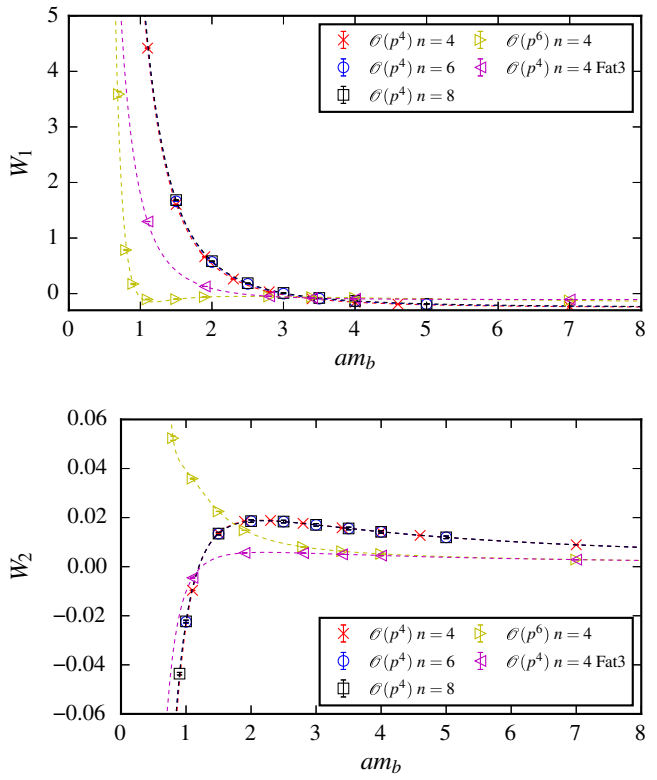

FIG. 3. Numerical values for W_1 (top) and W_2 (bottom) for different NRQCD actions without mean-field improvement as described in Sec. II.

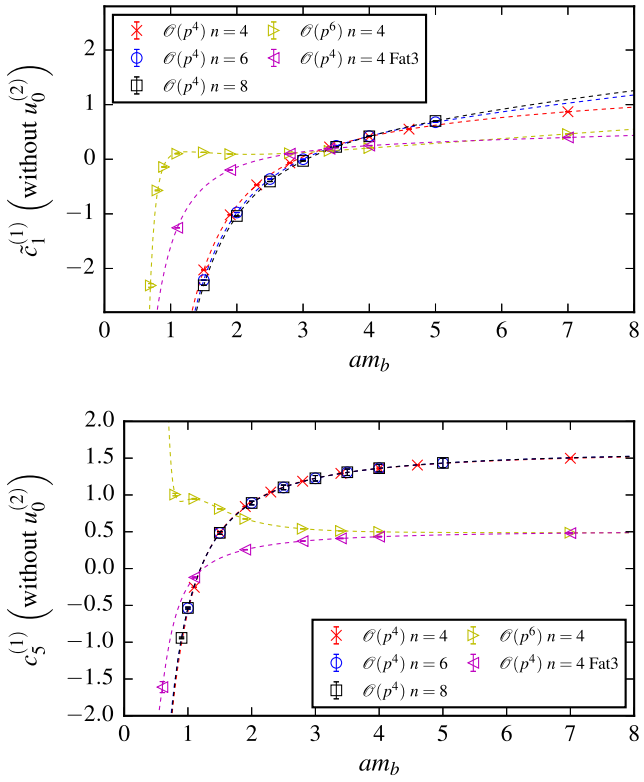

FIG. 4. Numerical values for $\tilde{c}_1^{(1)}$ (top) and $c_5^{(1)}$ (bottom) for different NRQCD actions without mean-field improvement.

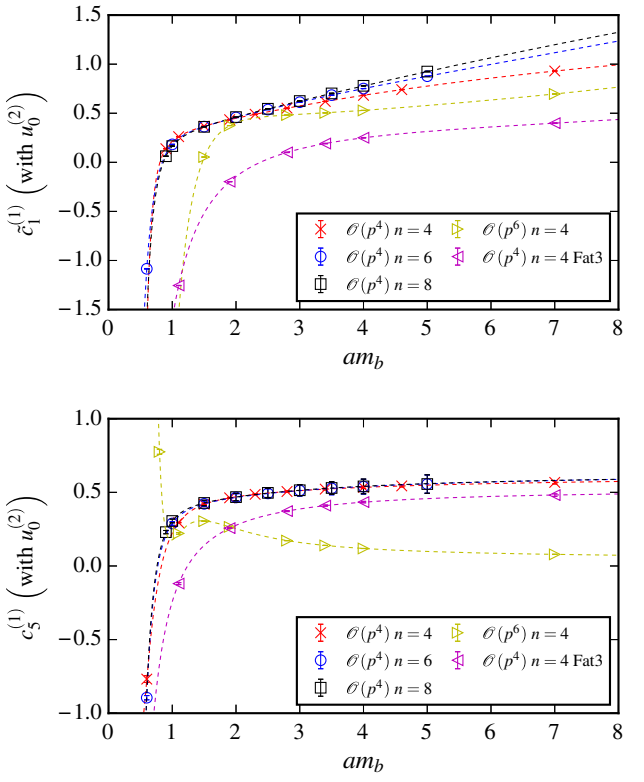

FIG. 5. As in Fig. 4 but with the mean-field improved data for $\tilde{c}_1^{(1)}$ (top) and $c_5^{(1)}$ (bottom). Note the change in vertical scale. The mean-field corrections are given in Appendix B. Note that the fat3 smeared data are the same as in Fig. 4, since no mean-field correction is applied in this case.

for our improved NRQCD action, indicating a breakdown of NRQCD, and that is clearly illustrated in our figures.

The difference between W_1 and W_2 in Fig. 3 and $\tilde{c}_1^{(1)}$ and $c_5^{(1)}$ in Fig. 4 is purely the conversion factors given in Eqs. (24) and (25). In these plots, a clear observation is that the results are very insensitive to an increase in n over the mass ranges that we are interested in for nonperturbative calculations on the lattice ($1 < am_b < 5$). Therefore, as there is no clear benefit to increase n in the perturbative results, future nonperturbative calculations can choose $n = 4$ for all am_b in this range. The fat3 smearing works as expected to remove the unphysical tadpoles (as outlined in Sec. II B), indicated by a reduction in the absolute size of the one-loop corrections. There is a significant improvement, in terms of longer plateau in am_b and sharper divergence at smaller am_b, when using the $\mathcal{O}(p^6)$ NRQCD action over the $\mathcal{O}(p^4)$. This improved behavior in the couplings leads to the expectation that the second-order couplings are also well-behaved.

In Fig. 5, we then include the mean-field tadpole corrections for all results (except those for fat3 smearing data) with the formulas explicitly given in Appendix B. The infinite-volume values are given in Table I. Table I shows why we do not need tadpole-improvement when smeared links are used. The one-loop coefficient in u_0 is much smaller in the smeared cases reflecting the fact that tadpole effects are much smaller and the mean smeared link is much closer to 1. Little is then gained by dividing by it.

As can be seen in Fig. 5, mean-field improvement noticeably reduces the magnitude of the one-loop coefficients, where it is applied. Due to the higher-order $1/am_b^n$ terms in the $\mathcal{O}(p^6)$ mean-field counterterms, as described in Sec. II B, the one-loop couplings with the $\mathcal{O}(p^6)$ action now diverge earlier as $am_b \to 0$. This is not a desirable feature. This common behavior is seen in all mean-field improved data we present. Interestingly, the absolute value of $c_5^{(1)}$ is significantly reduced when using a $\mathcal{O}(p^6)$ action. $c_5^{(1)}$ is the coupling which removes the rotational-symmetry breaking operator $\Delta^{(4)}$ at one-loop. Therefore, it is

TABLE I. The one-loop mean Landau gauge link [31] and its log moments for either an unsmeared or smeared gauge-link definition.

Gauge-link	$u_0^{(2)} = \langle f^{\mathrm{tad}} \rangle$	$\langle f^{\mathrm{tad}} \log(q^2) \rangle$	$\langle f^{\mathrm{tad}} \log^2(q^2) \rangle$
Unsmeared	0.750275(5)	1.45755(2)	3.6022(1)
Fat3	0.231784(5)	0.26101(7)	0.6429(2)
Fat7	0.108244(5)	0.10271(4)	0.4117(2)

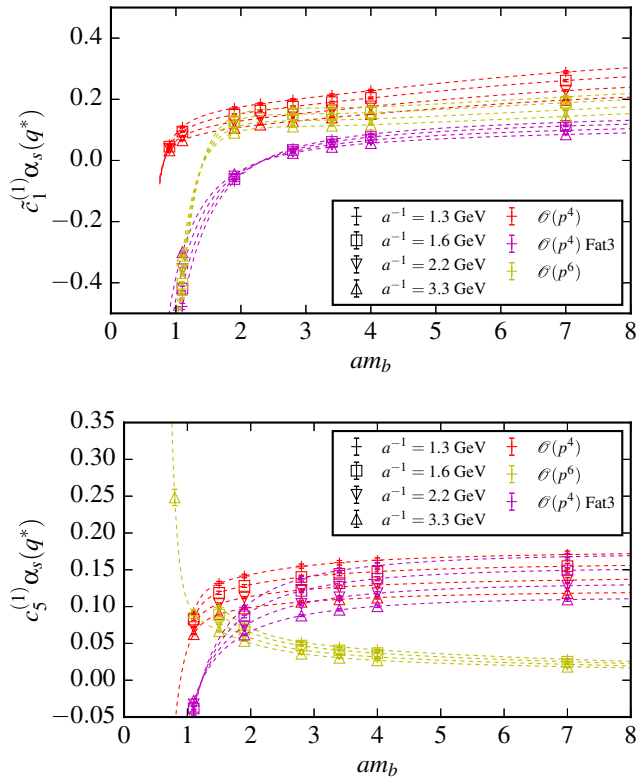

FIG. 6. The one-loop radiative correction $\tilde{c}_1^{(1)}\alpha_s(q^*)$ (top) and $c_5^{(1)}\alpha_s(q^*)$ (bottom) with α_s defined in the V-scheme, for different NRQCD actions and different values of the lattice spacings. We give a subset of the numerical values relevant for nonperturbative calculations in Appendix C.

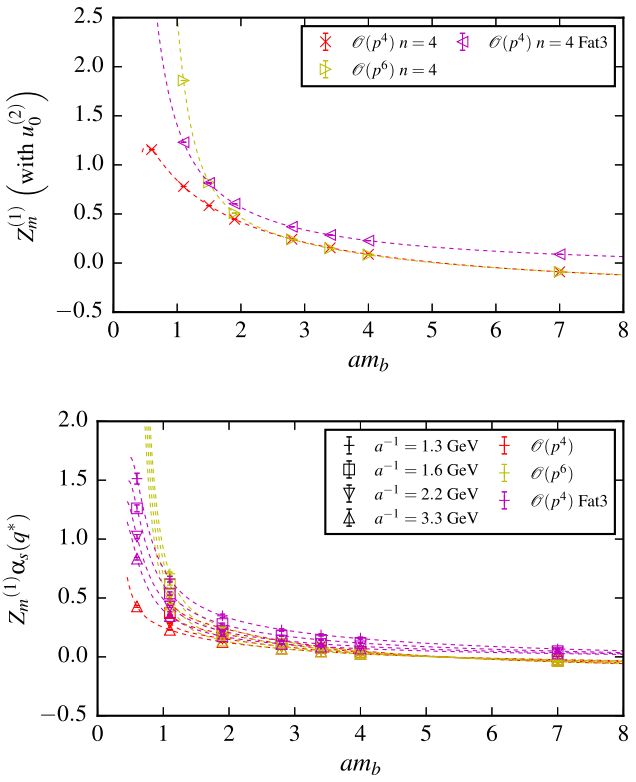

FIG. 7. Numerical values for $Z_m^{(1)}$ (top) and the one-loop radiative correction $Z_m^{(1)}\alpha_s(q^*)$ (bottom) with α_s defined in the V-scheme, for different NRQCD actions and different values of the lattice spacings. Note that the unsmeared data are mean-field improved as described Sec. II B, and the fat3 smeared results are not mean-field improved.

indicative that the $\mathcal{O}(p^6)$ action will reduce $SO(3)$ symmetry breaking in nonperturbative calculations also, as will be discussed in Sec. IV B.

To fully determine the one-loop shift to the kinetic couplings, the scale at which to evaluate α_s in the V-scheme needs to be found. We give the mean-field improved aq^* and the fat3 smeared aq^* in Appendix C. To determine the physical scale, q^*, we use $a^{-1} = 1.3$, 1.6, 2.2 and 3.3 GeV corresponding to very coarse, coarse, fine and superfine MILC ensembles used by the HPQCD Collaboration [3]. To run the strong coupling in a particular renormalization scheme, an initial condition needs to be chosen. Here, we use $\alpha_s^{\overline{\rm MS}}(M_Z, n_f = 5)$ taken from the Particle Data Group [1], where α_s is defined in the $\overline{\rm MS}$-scheme, M_Z is the Z-boson mass and $n_f = 5$ is the number of active flavors. To use this with our data, we perturbatively remove the b-quarks' contribution to the running [37], with $m_b(m_b) = 4.164(23)$ GeV [34], convert to the V-scheme [12,38] and run to q^* [39]. Finally, we combine $\alpha_V(q^*)$ with the one-loop coefficient to give the full one-loop coefficient. These are plotted in Fig. 6.

We show data for the tadpole-improved $Z_m^{(1)}$ in Fig. 7. Without mean-field improvement, the $\mathcal{O}(p^4)$ and $\mathcal{O}(p^6)$ data overlap very closely and are not shown due to this. The modified behavior after mean-field improvement is due to the different tadpole-corrections, where again, the $\mathcal{O}(p^6)$ tadpole-corrections cause faster divergences as $am_b \to 0$. The mean-field corrections work as expected to reduce the absolute value of $Z_m^{(1)}$, e.g., $Z_m^{(1)}(am_b = 1.9)$ is reduced from 1.57 (without improvement) to 0.45. The full one-loop correction is shown in the lower plot in the same figure.

W_0 is observed to have opposite sign to $Z_m^{(1)}$, but has similar qualitative features as those just described, e.g., the mean-field unimproved result is typically is a factor of 2–3 in magnitude larger than the mean-field improved values and there is a clear plateau and a sharp divergence at small am_b. The tadpole-improved W_0 is shown in Fig. 8.

Because $Z_m^{(1)}$ and W_0 have opposite sign, the one-loop shift in the zero of energy δC is found to be very close to zero in all cases as seen in Fig. 9.

We note that our $\mathcal{O}(p^4)$ $\tilde{c}_1^{(1)}$, $c_5^{(1)}$ and $Z_m^{(1)}$ differ by small but significant amounts from those in Ref. [3]. Reference [3] used Monte Carlo integration combined with numerical derivatives, which they note leads to unstable behavior when there are large peaks in the IR region.

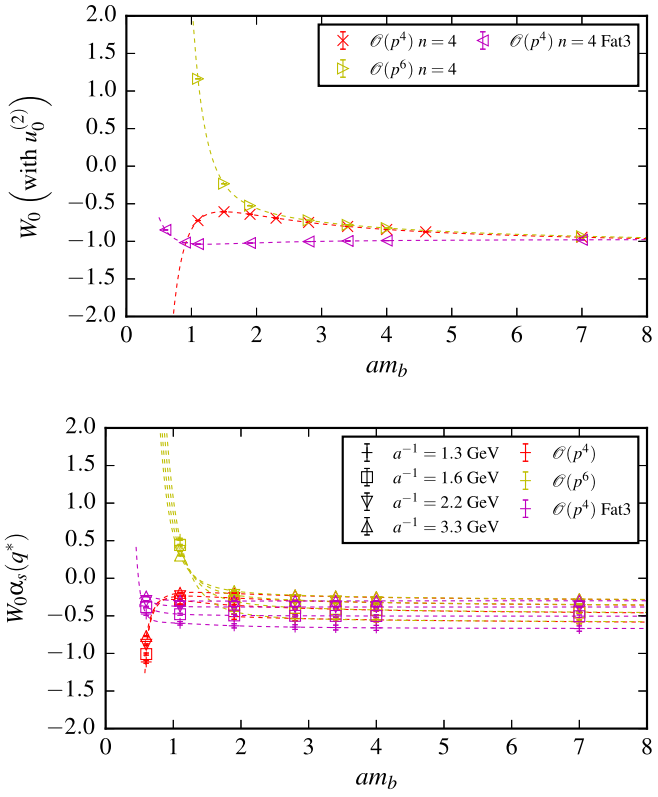

FIG. 8. The same as in Fig. 7 but for W_0 in place of $Z_m^{(1)}$.

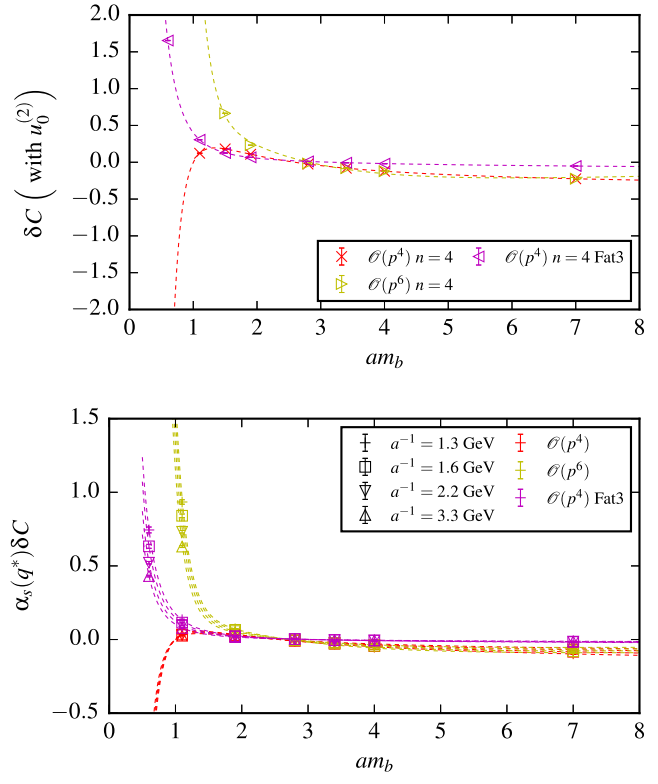

FIG. 9. The same as in Fig. 7 but with δC in place of $Z_m^{(1)}$.

Consequently subtraction functions were used [40]. In our study, we avoid these complications by using TBCs as a gauge-invariant IR regulator, and automatic differentiation for the derivatives, which avoids the numerical instabilities arising from finite-differencing schemes [26,32].

Finally, the tadpole-improved results for the one-loop coefficients plotted here are given in Appendix C. Subtracting the mean-field corrections (given in Appendix B) from this data gives the results before tadpole improvement.

IV. NONPERTURBATIVE KINETIC MASSES

Here we test how improving the NRQCD action as in Secs. II and III affects the reliability and accuracy of energies of bottomonium mesons obtained from nonperturbative calculations.

The static mass (the energy corresponding to zero spatial momentum) in lattice NRQCD is shifted due to the removal of the mass term from the Hamiltonian [3], where we found the one-loop shift, C, in Sec. II A. Consequently, one can only determine static mass differences fully nonperturbatively. However, one can still obtain kinetic masses [3,41] entirely nonperturbatively via a fully relativistic dispersion relation as

$$aM_{\text{kin}} = \frac{a^2\mathbf{P}^2 - a^2\Delta E^2}{2a\Delta E}, \tag{32}$$

where $a\Delta E$ is the energy difference between the meson with momentum $a\mathbf{P}$ and the meson at rest. The kinetic mass depends on the internal kinematics of the hadron, and hence on the kinetic terms in the NRQCD action. For example, changing the coefficient of the $(\Delta^{(2)})^2/8am_b^3$ term, c_1, from 1 to $1+\mathcal{O}(\alpha_s)$ will modify the amount of the internal kinetic energy that is incorporated into the meson's kinetic mass, effectively correcting for an $\mathcal{O}(\alpha_s)$ mismatch between the static and kinetic masses from this operator's contribution to the binding energy [3]. The change would be expected to be $\mathcal{O}(\alpha_s B)$ where B is the binding energy of $\mathcal{O}(500)$ MeV. This could in principle be as large as 150–200 MeV but in practice was found to be much smaller and around 80 MeV on coarse and fine lattices (because $c_1^{(1)}$ is small) [3].

Therefore, the kinetic mass is the ideal candidate on which to test our improvement of the kinetic part of the action. Furthermore, the kinetic mass is typically utilised to tune the b-quark mass [3,41–43], and thus if sizable improvement is seen, this would indicate that improving the kinetic action would benefit future calculations, where a highly accurate calculation with a reliable error budget requires knowledge of at least the $\mathcal{O}(\alpha_s)$ corrections to the matching coefficients.

In a rotationally invariant theory, the symmetry group is the semidirect product of the rotational group $SO(3)$ with three translations. The little group of the symmetry group,

TABLE II. The different little groups relevant for each momentum type in a finite-volume cubic lattice with PBC. The momenta are in units of $2\pi/L$ and n, m, p are nonzero integers with $n \neq m \neq p$ [44,45]. The single cover irreps describe integer spin states.

Momentum type	Little group (double cover)	Irreps (single cover)
(0, 0, 0)	O_h^D	$A_1^{\pm}, A_2^{\pm}, E^{\pm}, T_1^{\pm}, T_2^{\pm}$
$(n, 0, 0)$	Dic_4	A_1, A_2, E_2, B_1, B_2
$(n, n, 0)$	Dic_2	A_1, A_2, B_1, B_2
(n, n, n)	Dic_3	A_1, A_2, E_2
$(n, m, 0)$	C_4	A_1, A_2
(n, n, m)	C_4	A_1, A_2
(n, m, p)	C_2	A

used to classify energy eigenstates in terms of invariant quantities (e.g., J^P at zero-momentum and helicity λ at nonzero momentum), is broken by a finite-volume lattice [44]. The symmetry of the lattice discretization, which breaks $SO(3)$ symmetry at small distances, does not need to be the same as the symmetry of the finite volume, which breaks rotational symmetry at larger distances [45]. Here we consider a cubic lattice in a finite cubic box with PBCs, and so both the lattice and the boundary break the full $SO(3)$ rotational symmetry of the continuum to the (double cover) of the octahedral group, O_h^D. The lattice irreducible representations (irreps) for a cubic finite-volume on a cubic lattice depend on the allowed momenta types [44,45] (as not all lattice-momenta are related by an octahedral symmetry), and we reproduce them in Table II for convenience. The energy eigenstates of the lattice Hamiltonian (as obtained from nonperturbative lattice QCD calculations) are classified according to representations of the lattice symmetry group.

We denote the energy computed on the lattice for a η_b meson with spatial momentum P as $E_{\eta_b}(|aP|)$. Then $E_{\eta_b}(|a\mathbf{P}|)$ computed with the same $a^2\mathbf{P}^2$ but with $a\mathbf{P}$ which lie in different lattice little groups [e.g., (3, 0, 0) which has little group Dic_4 and (2, 2, 1) which has little group C_4] do not need to yield the same energy within errors. However, as the infinite-volume continuum limit is taken and full $SO(3)$ symmetry is restored, these energies should converge. Improving the lattice NRQCD action, both by adding in higher-order $\mathcal{O}(p^6)$ terms and one-loop radiative corrections, should reduce $SO(3)$ symmetry breaking and produce the desired infinite-volume continuum energies more accurately at a given value of the lattice spacing. Examining the nonperturbative energies should indicate this to be the case.

Improving the NRQCD action will reduce the breaking of $SO(3)$ symmetry due to a cubic lattice. This is because higher-order rotational-symmetry breaking operators (which vanish as $a \to 0$) will be increasingly taken into account correctly, e.g., the $\sum_i \Delta_i^4, \sum_{i,j} \Delta_i^2 \Delta_j^4, \sum_i \Delta_i^6$ operators in Eq. (2). It is perhaps indicative that including $\mathcal{O}(p^6)$ operators reduces rotational symmetry breaking, as we found in Sec. III B that the one-loop coupling $c_5^{(1)}$, which is constructed in (25) to remove the rotational-symmetry breaking $\sum_i p_i^4$ terms from the dispersion relation to one-loop, gets reduced when improving to the $\mathcal{O}(p^6)$ NRQCD action.

In the following we will describe our nonperturbative computational setup as well as discuss how the data from the kinetic masses illustrates the reduction of $SO(3)$ symmetry breaking when improving the kinetic parts of the NRQCD action.

A. Nonperturbative computational setup

Our computational setup is similar to that in Refs. [3,8], and we point the reader to those texts for specific details. However, we give a brief overview. We use gauge ensembles generated by the MILC Collaboration [46] with the tadpole-improved Lüscher-Weisz gauge action [47] with $2+1+1$ dynamical flavors of HISQ sea quarks [15]. Details of these ensembles are given in Table III. We use ensembles at three values of the lattice spacing, approximately 0.15 fm, 0.12 fm and 0.09 fm, so that we can test the changing impact of lattice discretization effects.

Details of the covariant derivative and chromomagnetic/electric field implementation in our NRQCD action can be found in [3]. Each of these must be tadpole-improved using the same improvement procedure as in the perturbative calculation of the matching coefficients in Sec. III B. We present kinetic masses using the mean-field improvement procedure where, as in the perturbative results, we take u_0 as the mean trace of the gluon field in Landau gauge, calculated in [3,6]. The u_0 values used for each ensemble are given in Table IV. We also give in Table IV the values that we use for the bare b quark mass am_b on each ensemble.

The lattice two-point correlator most naturally encodes information on meson energies. We use bilinear $b\bar{b}$ interpolating operators, listed in Table V with $\Gamma = i\gamma_5, \gamma^j$, which

TABLE III. Details of the gauge ensembles used in this study. β is the gauge coupling. a_Υ is the lattice spacing determined from the $\Upsilon(2S-1S)$ splitting [3], where the error combines statistics, experiment and the dominant NRQCD systematic error. am_q are the sea quark masses, $N_s \times N_T$ gives the spatial and temporal extent of the lattices in lattice units and n_{cfg} is the number of configurations in each ensemble. In column 1 we use the numbering convention for the ensembles from [3]. Ensemble 1 is referred to as "very coarse", 3 as "coarse," and 5 as "fine".

Set	β	a_Υ (fm)	am_l	am_s	am_c	$N_s \times N_T$	n_{cfg}
1	5.8	0.1474(15)	0.013	0.065	0.838	16×48	1020
3	6.0	0.1219(9)	0.0102	0.0509	0.635	24×64	1052
5	6.3	0.0884(6)	0.0074	0.037	0.440	32×96	1008

TABLE IV. Parameters used for the valence quarks. am_b is the bare b-quark mass in lattice units, u_{0L} is the tadpole parameter [8]. T_p is the total propagation time for the b-quark propagator and n_t is the number of time sources used per configuration. The $\mathcal{O}(\alpha_s)$ matching coefficients for c_1, c_6 and c_5 are taken from Tables VIII and IX. As explained in Sec. III the $\mathcal{O}(\alpha_s)$ coefficients are functions of am_b; the α_s value they are combined with to give c_1, c_5 and c_6 depends on the lattice spacing. The values are different for each version of the NRQCD action tested. As we focus on the improvements made in this study, c_2, c_3 and c_4 are taken to be their tree-level values of 1.0.

Set	am_b	u_{0L}	T_p	n_t
1	3.40	0.8195	40	16
3	2.80	0.8349	40	16
5	1.90	0.8525	48	16

TABLE V. The local bilinear operators used in this study. Note the $i\gamma^5$ is needed to make the overlaps real [48]. The second column gives the J^{PC} states that these operators create at rest in an infinite volume continuum. The third column gives the helicity eigenvalues λ that these operators create at nonzero momentum in an infinite volume continuum which is only rotationally invariant, while the J in brackets are the states which contribute to that helicity (cf. [8,45]).

$\mathcal{O}^\Gamma(x)$	J^{PC}	$\lambda(\leftarrow J^P)$
$\bar{\psi} i\gamma^5 \psi$	0^{-+}	$0^-(\leftarrow J^P = 0^-, 1^+, 2^-, \ldots)$
$\bar{\psi}\gamma^i\psi$	1^{--}	$0^+(\leftarrow J^P = 0^+, 1^-, 2^+, \ldots)$ $\lvert 1\rvert(\leftarrow J = 1, 2, 3, \ldots)$

overlap onto definite $J^{PC} = 0^{-+}, 1^{--}$ energy eigenstates at rest, respectively, in the infinite-volume continuum version of our theory (which is rotationally invariant) [45]. In [8], as well as [45], it has been shown that at nonzero momentum, $\mathcal{O}^{\gamma^5}(p)$ is a helicity operator which creates a definite $\lambda = 0^-$ energy eigenstate, but $\mathcal{O}^{\gamma^i}(p)$ creates an admixture of $\lambda = 0^+, \pm 1$, where these λ get contributions from J^P values as listed in the third column of Table V. The $\pm$ superscript on the $\lambda = 0$ case represents the eigenvalue $\tilde{\eta} = P(-1)^J$ from the $\hat{\Pi}$ symmetry (a parity transformation followed by a rotation to bring the momentum direction back to the original direction) [45].

Again, following [3], we simultaneously fit multiexponential functions to the bottomonium meson correlator at rest and with momentum $a\mathbf{P}$. Doing so allows the correlations between the ground states energies to be correctly taken into account when computing the kinetic mass. We take priors of 0.1(1.0) on the amplitudes, priors on the ground state energies are estimated from previous results and given a suitably wide width [3], and priors on energy splittings are taken to be $E_{n+1} - E_n = 500(250)$ MeV. To help invert the covariance matrix a singular value decomposition is used with a tolerance of 10^{-5} [8,49]. We present fit results, following [3], for fits including eleven exponentials for set 1, nine exponentials for set 3, and seven exponentials for set 5.

B. Nonperturbative results and analysis

We generate data for $E_{\eta_b}(|a\mathbf{P}|)$ and $E_\Upsilon(|a\mathbf{P}|)$ with momenta $a\mathbf{P} = (0,0,0)$, (1, 0, 0), (1, 1, 0), (1, 1, 1), (2, 0, 0), (2, 1, 1), (2, 2, 1) and (3, 0, 0) in multiples of $2\pi/L$. As discussed above, helicity classifies the energy eigenstates of the infinite-volume continuum NRQCD theory at nonzero momentum. Therefore, compared to the zero-momentum case, additional J^P states can contribute to the correlator data at nonzero momentum. The authors of [8] found that when fitting to a 3×3 matrix of smeared correlators, the first excited state in the fit at nonzero momentum was the $\chi_{b1}(1P)$, $h_b(1P)$ for the operators $\mathcal{O}^{\gamma^5}(x)$, $\mathcal{O}^{\gamma^i}(x)$ respectively. At zero momentum, the first excited state was the $\eta_b(2S)$, $\Upsilon(2S)$ respectively. By using the same smearing types and correlators as those authors, we check that the additional states are present at nonzero momentum when using a 3×3 fit. However even when a fit does not resolve the additional (first excited) state accurately we find that the ground state is uncontaminated and still precise. Further, the finite-volume lattice breaks $SO(3)$ symmetry and allows mixing with higher J^P states within each of the lattice irreps given in Table II. As in [8], we find no signal for any mixing in the low-lying spectrum. We conclude that our ground state energies are reliably determined.

Each $E_\Upsilon(|a\mathbf{P}|)$ extracted from our lattice calculation has larger errors than those on $E_{\eta_b}(|a\mathbf{P}|)$ because of the slightly poorer signal-to-noise ratio. The statistical errors also grow with momentum. Consequently, $\Delta E(|a\mathbf{P}|)$ has larger absolute errors as $a^2\mathbf{P}^2$ grows, but the relative error on $\Delta E(|a\mathbf{P}|)$ is larger for small $a^2\mathbf{P}^2$. As a result, the kinetic masses with smaller $a^2\mathbf{P}^2$ have larger errors, which then stabilize.

On each ensemble we examine the kinetic mass, given by Eq. (32), in order to see how the kinetic mass changes for a given am_b as a function of momentum, as we improve the NRQCD action. Since the energies and kinetic masses should only depend on the magnitude of the spatial momentum, rotational symmetry breaking effects show up most clearly as a difference between the energies corresponding to momenta (3, 0, 0) and (2, 2, 1) in units of $2\pi/L$, and also as a kinetic mass that depends on $a^2\mathbf{P}^2$.

One feature of the results is that the kinetic mass for the η_b is slightly larger than that of the Υ, rather than being lower to reflect the ordering of the masses seen in experiment. This was also seen in [3] and explained there as the result of not including relativistic corrections to the $\sigma \cdot B/2m$ term in the NRQCD action [the term with coefficient c_4 in Eq. (3)]. Such corrections [spin-dependent terms at $\mathcal{O}(v^6)$] would allow the effect of the $\sigma \cdot B$ term to be

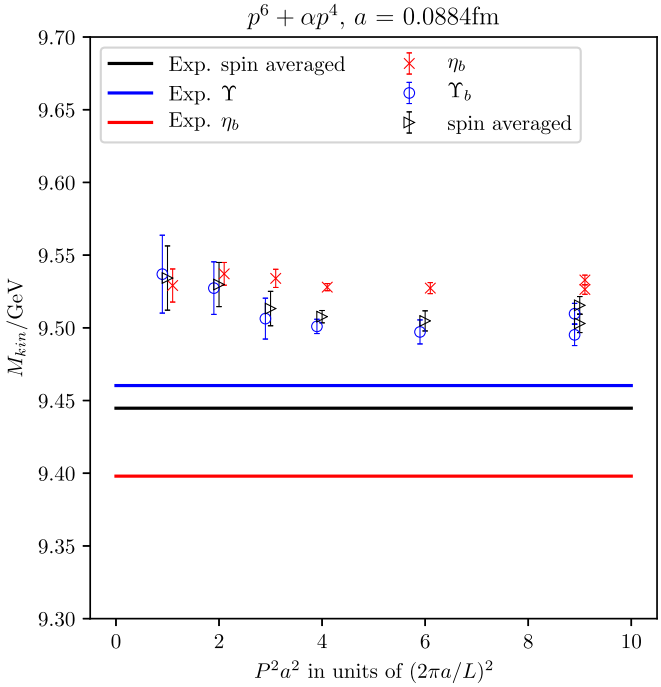

FIG. 10. Nonperturbatively obtained values for $M_{\rm kin}$ for the η_b and the Υ plotted against momentum squared, together with the spin-averaged kinetic mass, on set 5. The solid lines show experimental values and errors are statistical only.

correctly incorporated in the kinetic mass and solve this problem [9,10]. The strategy adopted in [3] to mitigate this problem was to use the spin-averaged kinetic mass, which is less sensitive to these effects, to tune the b quark mass. The spin-averaged kinetic mass is given by

$$M_{\rm kin}^{\text{spin-averaged}} = \frac{3M_{\rm kin,\Upsilon} + M_{\rm kin,\eta_b}}{4}. \tag{33}$$

Figure 10 illustrates this feature by showing results for the Υ and η_b kinetic masses on set 5, for the $p^6 + \alpha_s p^4$ action. We also show the spin-averaged kinetic mass. The solid lines show the corresponding experimental values. In a full nonperturbative calculation we would want to tune the am_b value for each action separately to match the spin-averaged kinetic mass to experiment. Here however we keep the same am_b value for each action on a given ensemble (with only an approximate tuning) so that we can compare how the kinetic mass changes.

Data for the spin-averaged kinetic masses from the tree-level $\mathcal{O}(p^4)$ and $\mathcal{O}(p^6)$ NRQCD actions, both with and without $\mathcal{O}(\alpha_s p^4)$ corrections, are presented in Figs. 11 and 12 for the ensembles described in Table III. Errors are statistical only. Since these plots have the same vertical scale we can see a reduction in the size of ap^6 and $\mathcal{O}(\alpha_s)$ effects as the lattice spacing is reduced, from the fact that the range of results become more compressed from sets 1 to 5.

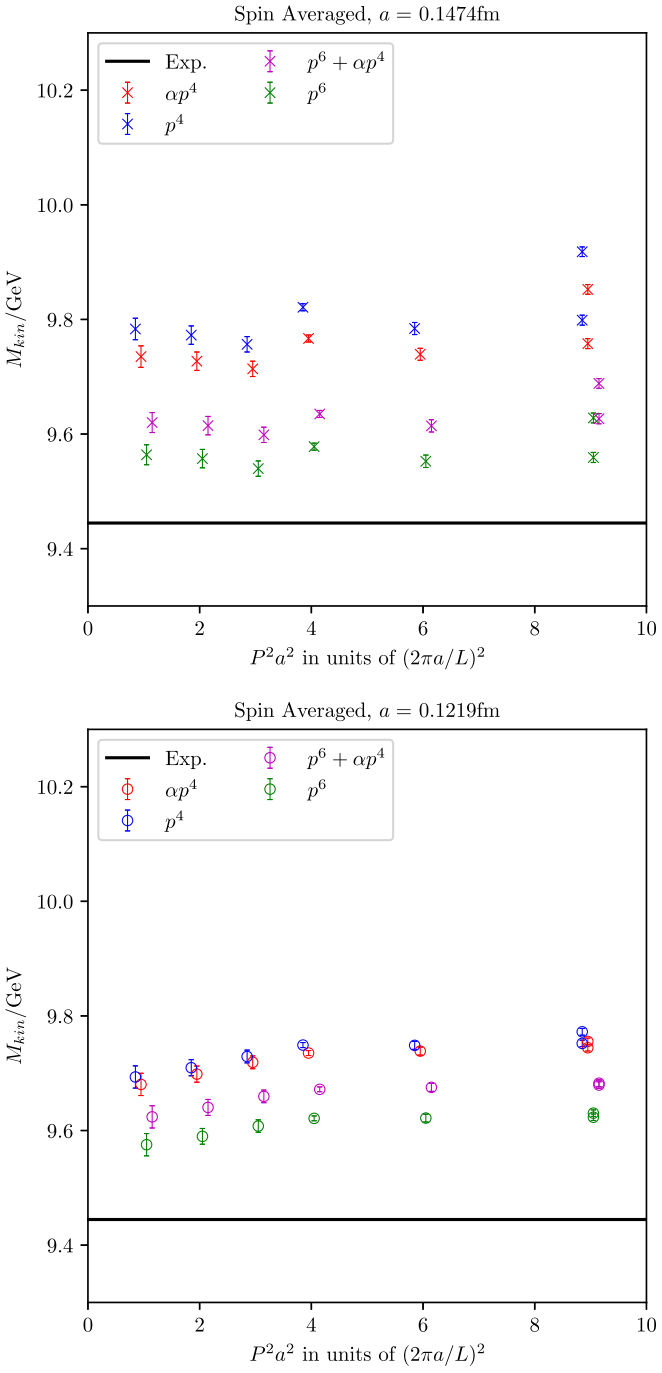

FIG. 11. Nonperturbatively obtained spin-averaged kinetic masses, given by Eq. (33), on very coarse set 1 (above) and coarse set 3 (below) for p^4 and p^6 actions with both tree-level and $\mathcal{O}(\alpha_s)c_1, c_6$ and c_5. The errors shown are statistical only, excluding lattice spacing uncertainty, and are correlated. The data points at each value of P^2a^2 have been offset symmetrically for clarity. The larger energy with $a|\mathbf{P}| = 9$ is from the (2, 2, 1) ground state. The solid line is the experimental value.

In Fig. 13 we plot the differences between the energies of η_b states with momentum (2, 2, 1) and (3, 0, 0), in units of $2\pi/L$, on each ensemble using different actions. We see that the largest $SO(3)$ breaking occurs for the $\mathcal{O}(p^4)$

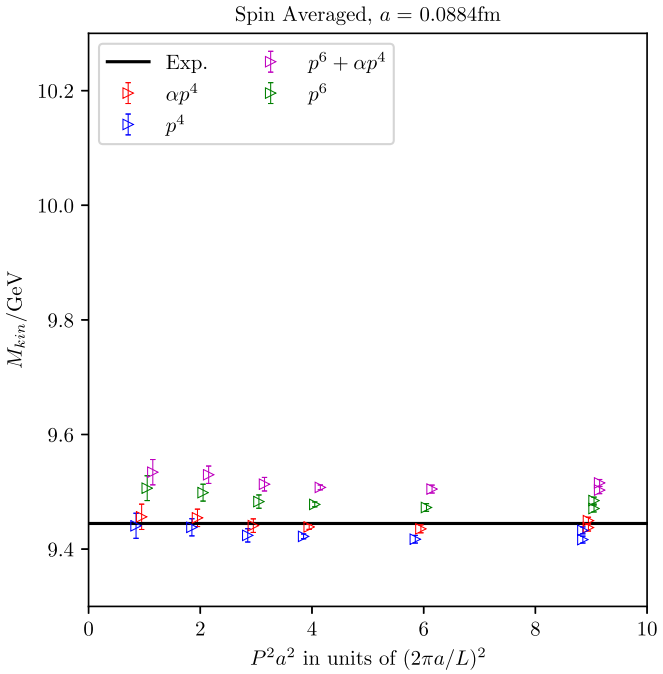

FIG. 12. Same as Fig. 11 but on fine set 5.

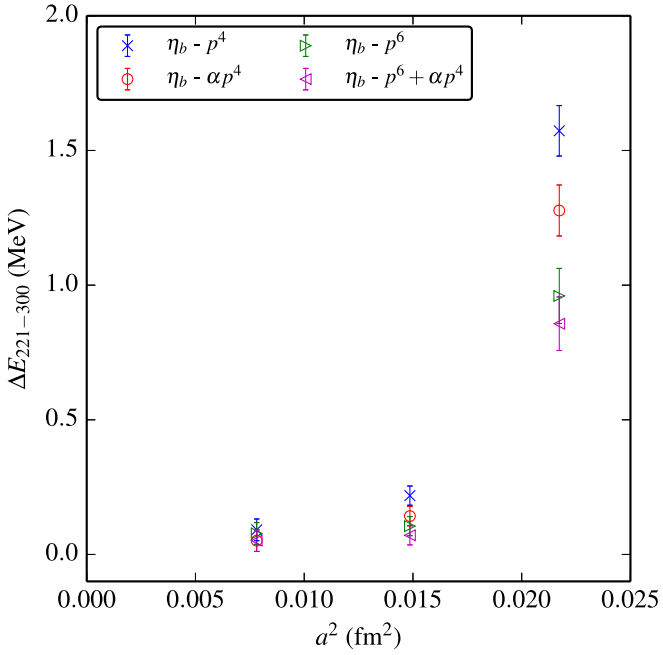

FIG. 13. Nonperturbatively obtained values for $\Delta E_{221-300}$ for the η_b for each action plotted against the square of the lattice spacing.

NRQCD action. This breaking is reduced when including the $\mathcal{O}(\alpha_s p^4)$ kinetic couplings, and then reduced further by the $\mathcal{O}(p^6)$ NRQCD action. The least $SO(3)$ breaking occurs for the $\mathcal{O}(\alpha_s p^4, p^6)$ NRQCD action. This improvement is sizable for the very coarse ensemble, set 1, while for the coarse and fine ensembles the improvement is visible,

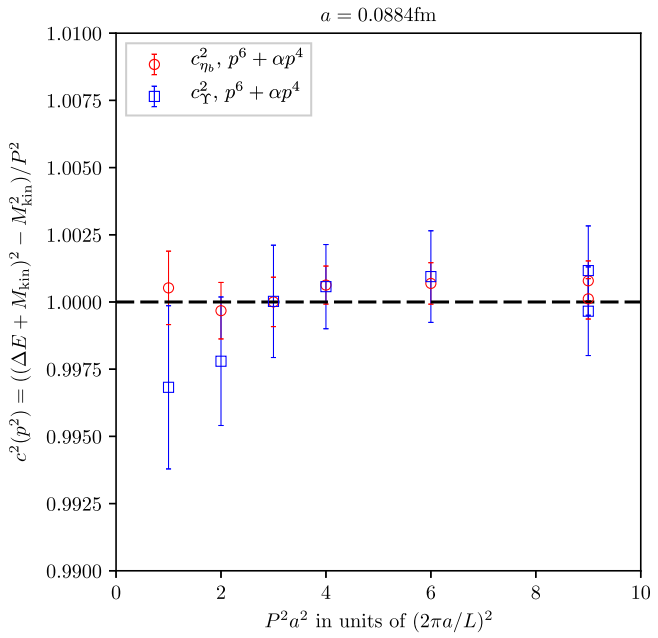

FIG. 14. The speed of light squared, $c^2P^2 = (\Delta E + M_{\rm kin})^2 - M^2_{\rm kin}$, on set 5 with the $\mathcal{O}(\alpha_s p^4, p^6)$ NRQCD action. The errors shown are statistical only, and we use the value of $M_{\rm kin}$ computed using momentum (1, 1, 1). The dashed line corresponds to $c^2 = 1$.

but small. Further, the breaking on the coarse and fine ensembles goes from being a significant effect to a nonsignificant (2σ) one after improvement. Using this improved action allows for a more accurate and reliable determination of the kinetic mass, and hence also of the tuned b-quark mass in high precision calculations.

In Fig. 14, we show the speed of light squared, $c^2 = ((\Delta E + M_{\rm kin})^2 - M^2_{\rm kin})/P^2$, computed on set 5 with the $\mathcal{O}(\alpha_s p^4, p^6)$ NRQCD action against P^2a^2, where good agreement with the value of 1 is seen.

V. DISCUSSION AND CONCLUSIONS

In this work we have made the next round of improvement to the HPQCD Collaboration's formulation of the NRQCD action to allow increasingly accurate nonperturbative calculations in the future. The key results presented herein include:

(i) Determining the required operators which need to be added to the NRQCD action in order to give a correct heavy-quark dispersion relation to $\mathcal{O}(p^6)$, presented in Sec. II.

(ii) Determining the one-loop coefficients of the $\mathcal{O}(p^4)$ kinetic couplings, namely $c_1^{(1)}, c_6^{(1)}$ and $c_5^{(1)}$, in automated lattice perturbation theory using twisted boundary conditions as an IR regulator. We also present results for the one-loop (bare-to-pole) heavy-quark mass renormalization $Z_m^{(1)}$ and zero-point

energy W_0 which can be combined to give the one-loop energy shift (from neglecting the quark mass term in the NRQCD action) of a b-quark. This one-loop energy shift can be added to the nonperturbatively determined simulation energies to give a numerical value, which after converting to GeV, can be compared to the experimentally determined masses. All perturbative results are shown in Sec. III B.

(iii) Determining the full one-loop radiative correction of these quantities by finding the scale q^* of α_s defined in the V-scheme. In doing this we use the higher order methodology which takes into account the anomalously small leading-order moments in order to obtain physical q^* as described in Sec. II B.

(iv) Determining the one-loop quantities for three different NRQCD action formulations, namely a NRQCD action that gives a heavy-quark dispersion relation correct (i) to $\mathcal{O}(p^4)$ and (ii) to $\mathcal{O}(p^6)$. These actions employ a mean-field tadpole improvement procedure. For reasons described in Sec. II B we also explore, for the first time, a (iii) fat3 smeared NRQCD action with the quark dispersion relation correct to $\mathcal{O}(p^4)$ which does not require mean-field improvement. The fat3 results are encouraging and show stable behavior against am_b, indicating that the use of this or a similar smearing may be the way forward in future, rather than tadpole-improvement.

(v) Varying the stability parameter with $n = 4$, 6 and 8 to show that, as shown in Sec. III B, the $\mathcal{O}(\alpha_s p^4)$ kinetic couplings in the NRQCD action are insensitive to this choice. Thus, if future calculations need to compensate a decrease in lattice spacing (which allows higher momentum fluctuations) with an increase in n, they can do so reliably.

(vi) Testing how the improvement of the NRQCD action, both in terms of additional $\mathcal{O}(p^6)$ operators and one-loop radiative kinetic coefficients, affects the nonperturbatively obtained kinetic masses, c. f. Figs. 11–13. The impact of the p^6 terms and the radiative corrections on the kinetic masses obtained is small, particularly on the finer lattices. We find a significant reduction in $SO(3)$ symmetry breaking when using the improved actions on the very coarse ensemble, set 1, which decreases as the lattice spacing is reduced. On the fine lattice, set 5, $SO(3)$ symmetry breaking has been reduced to the point that the energy splitting, shown in Fig. 13, is very nearly consistent with zero.

Taken together, NRQCD allows increasingly accurate and precise numerical calculations to be performed by including higher-order operators, in combination with determining the matching coefficients using perturbation theory. We have taken both these steps in this work. Furthermore, NRQCD is numerically cheap compared to its relativistic counterparts, being an initial-value, rather than a boundary-value problem. The outlook for NRQCD in the high-precision era is promising and this work helps ensure that this NRQCD formalism will continue to be an active contributor.

ACKNOWLEDGMENTS

We would like to thank Christopher Thomas for the many insightful discussions on finite-volume lattice effects. We are also grateful to the MILC Collaboration for the use of their gauge configurations. This manuscript has been authored by Fermi Research Alliance, LLC under Contract No. DE-AC02-07CH11359 with the U.S. Department of Energy, Office of Science, Office of High Energy Physics. This work was funded in part by UK Science and Technology Facilities Council (STFC) Grants No. ST/L000385/1, No. ST/L000466/1, and No. ST/P000681/1. This work used the DiRAC Data Analytic system at the University of Cambridge, operated by the University of Cambridge High Performance Computing Service on behalf of the STFC DiRAC HPC Facility (www.dirac.ac.uk). This equipment was funded by the department of Business, Innovation and Skills, UK. National E-infrastructure capital grant (Grant No. ST/K001590/1), STFC capital Grants No. ST/H008861/1 and No. ST/H00887X/1, and STFC DiRAC Operations Grant No. ST/K00333X/1. DiRAC is part of the National E-Infrastructure.

APPENDIX A: DERIVATIVE CONVENTIONS

In this section we define our convention for the discretized derivative operators for use in the perturbative and nonperturbative calculations. The forward, backward and partially cancelled second-order $\Delta_j^{(2)}$ operator are given by [note that all gauge-links are implicitly mean-field improved so that $U_i(x)$ is replaced by $U_i(x)/u_0$]

$$\Delta_i^+(x) = U_i(x)\psi(x+i) - \psi(x), \tag{A1}$$

$$\Delta_i^-(x) = \psi(x) - U_{-i}(x)\psi(x-i), \tag{A2}$$

$$\Delta_j^{(2),PC}\psi(x) = U_j(x)\psi(x+j) + U_j^\dagger(x-j)\psi(x-j) - 2\psi(x). \tag{A3}$$

Then our partially corrected operators are

$$\Delta^{(2)} = \sum_j \Delta_j^{(2),PC}, \tag{A4}$$

$$\Delta^{(4)} = \sum_j \Delta_j^{(2),PC}\Delta_j^{(2),PC}, \tag{A5}$$

$$\Delta^{(6)} = \sum_j \Delta_j^{(2),PC}\Delta_j^{(2),PC}\Delta_j^{(2),PC}, \tag{A6}$$

$$\Delta^{(2)}\Delta^{(4)} = [\Delta^{(2)}][\Delta^{(4)}] + \left(1 - \frac{1}{u_0^2}\right)(\Delta^{(2)} - 18), \quad \text{(A7)}$$

$$(\Delta^{(2)})^2 = [\Delta^{(2)}]^2 + 6\left(1 - \frac{1}{u_0^2}\right), \quad \text{(A8)}$$

$$(\Delta^{(2)})^3 = [\Delta^{(2)}]^3 + \left(1 - \frac{1}{u_0^2}\right)(11\Delta^{(2)} - 42). \quad \text{(A9)}$$

The additional terms in Eqs. (A7), (A8) and (A9) are needed for the partial cancellation as described in Sec. II B. As can be seen, when the operators are transformed to momentum space, the additional terms in these partially cancelled operators allow mixing down of higher-order coefficients to lower-order tadpole counterterms. For the smeared operators, no mean-field improvement is performed (i.e. u_0 is set to 1) so the additional terms vanish and the links are replaced by their smeared counterparts.

APPENDIX B: TADPOLE COUNTERTERMS FROM MEAN-FIELD IMPROVEMENT

In this appendix we will give explicit formulas for the tadpole counterterms used to remove the unphysical tadpole contributions, as described in Sec. II B, when using a mean-field improvement procedure. These formulas are utilized to produce the one-loop mean-field improved quantities discussed in Sec. III B. Features of these formulas have been discussed in Sec. II B.

For a $\mathcal{O}(p^4)$ NRQCD action [e.g., using Eq. (2) with $\delta H_{p^6} = 0$] with partial cancellation, the tadpole counterterms are

$$\begin{aligned}
\frac{Z_m^{(1),\mathrm{tads}}}{u_0^{(2)}} &= -\frac{2}{3} - \frac{3}{m_b^2}, \\
\frac{\tilde{c}_1^{(1),\mathrm{tads}}}{u_0^{(2)}} &= -\frac{1}{8}\left(1 + \frac{m_b}{2n}\right)^{-1}\left[\frac{12}{n^2} - \frac{1}{n} + \frac{1}{2m_b}\left(\frac{3}{n^2} - 4\right) + \frac{6}{m_b^2}\left(\frac{1}{n} - 12\right) + \frac{6}{m_b^3}\right], \\
\frac{c_5^{(1),\mathrm{tads}}}{u_0^{(2)}} &= -\frac{4}{3} + \frac{1}{4m_b} + \frac{3}{m_b^2} - \frac{3}{8nm_b^2} - \frac{3}{4m_b^3}, \\
\frac{W_0^{\mathrm{tads}}}{u_0^{(2)}} &= 1 + \frac{7}{2m_b} - \frac{3}{2m_b^2}\left(1 + \frac{m_b}{2n}\right).
\end{aligned} \quad \text{(B1)}$$

For a $\mathcal{O}(p^6)$ NRQCD action [e.g., using Eq. (2)] with partial cancellation, the tadpole counterterms are

$$\begin{aligned}
\frac{Z_m^{(1),\mathrm{tads}}}{u_0^{(2)}} &= -\frac{3}{5} - \frac{43}{12m_b^2} + \frac{11}{4m_b^4}\left(1 - \frac{m_b^2}{6n^2}\right), \\
\frac{W_0^{\mathrm{tads}}}{u_0^{(2)}} &= 1 + \frac{37}{10m_b} - \frac{3}{4nm_b^2} - \frac{9}{4m_b^3} + \frac{21}{4m_b^5}\left(1 - \frac{m_b^2}{6n^2}\right),
\end{aligned} \quad \text{(B2)}$$

$$\begin{aligned}
\frac{\tilde{c}_1^{(1),\mathrm{tads}}}{u_0^{(2)}} &= -\frac{1}{8}\left(1 + \frac{m_b}{2n}\right)^{-1}\left[-\frac{56}{15} - \frac{7}{5n} + \frac{1}{2m_b}\left(\frac{3}{n^2} - \frac{28}{5}\right) + \frac{1}{2m_b^2}\left(\frac{15}{n} - 28\right) + \frac{9}{m_b^3} + \frac{66}{m_b^4}\left(1 - \frac{m_b^2}{6n^2}\right)\right. \\
&\quad \left. - \frac{21}{m_b^5}\left(1 - \frac{m_b^2}{6n^2}\right) - \frac{21}{2nm_b^4}\left(1 - \frac{m_b^2}{6n^2}\right)\right], \\
\frac{c_5^{(1),\mathrm{tads}}}{u_0^{(2)}} &= -\frac{3}{5} + \frac{7}{20m_b} + \frac{1}{m_b^2}\left(\frac{7}{12} - \frac{3}{8n}\right) - \frac{9}{8m_b^3} - \frac{11}{4m_b^4}\left(1 - \frac{m_b^2}{6n^2}\right) + \frac{21}{8m_b^5}\left(1 - \frac{m_b^2}{6n^2}\right).
\end{aligned} \quad \text{(B3)}$$

APPENDIX C: NUMERICAL RESULTS

In this section, we give numerical values for the tadpole-improved one-loop coefficients in Table VI. The tadpole counterterms given in Appendix B can be used with the mean-field improved data to produce the raw results. We also give aq^* in Table VII for each quantity which is used to determine the value of α_V. Lastly, a subset of the full one-loop radiative corrections relevant for heavy-quark nonperturbative calculations are given in Tables VIII and IX. Other values can be read off the figures in Sec. III B.

TABLE VI. Numerical values of the one-loop coefficients. Note that the unsmeared results [$\mathcal{O}(p^4)$ and $\mathcal{O}(p^6)$] are mean-field improved given the formulas in Appendix B and the mean field parameter in Table I. The smeared results (fat3) are not mean-field improved.

am_b	7.0	4.0	3.4	2.8	1.9	1.1
$\tilde{c}_1^{(1)}$						
$\mathcal{O}(p^4)$	0.93051(24)	0.68266(17)	0.61998(16)	0.55180(13)	0.43443(15)	0.261360(99)
$\mathcal{O}(p^6)$	0.69607(24)	0.52875(17)	0.50348(16)	0.48171(13)	0.37427(10)	−1.5525(50)
Fat3	0.3991(37)	0.2504(27)	0.1914(24)	0.1012(21)	−0.1970(15)	−1.25492(97)
$c_5^{(1)}$						
$\mathcal{O}(p^4)$	0.568(11)	0.5341(62)	0.5220(53)	0.5056(44)	0.4628(30)	0.2946(17)
$\mathcal{O}(p^6)$	0.07863(55)	0.11875(32)	0.13945(27)	0.17215(22)	0.26557(15)	0.2212(58)
Fat3	0.4813(87)	0.4338(50)	0.4100(42)	0.3727(35)	0.2569(24)	−0.1199(69)
$Z_m^{(1)}$						
$\mathcal{O}(p^4)$	−0.08945(52)	0.08892(52)	0.15488(52)	0.24259(52)	0.44572(52)	0.77983(52)
$\mathcal{O}(p^6)$	−0.08988(52)	0.08413(52)	0.14947(52)	0.24053(52)	0.50827(52)	1.85962(52)
Fat3	0.08866(52)	0.22842(52)	0.28608(52)	0.36957(52)	0.60455(52)	1.23018(52)
W_0						
$\mathcal{O}(p^4)$	−0.94595(52)	−0.84252(52)	−0.80232(52)	−0.74890(52)	−0.64040(52)	−0.72316(52)
$\mathcal{O}(p^6)$	−0.93235(52)	−0.82391(52)	−0.78118(52)	−0.72050(52)	−0.52587(52)	1.16267(52)
Fat3	−0.97946(52)	−0.98997(52)	−0.99508(52)	−1.00270(52)	−1.02215(52)	−1.03670(52)
δC						
$\mathcal{O}(p^4)$	−0.22458(53)	−0.12171(54)	−0.08110(54)	−0.02487(55)	0.10867(59)	0.12242(70)
$\mathcal{O}(p^6)$	−0.22307(53)	−0.12185(54)	−0.08029(54)	−0.01679(55)	0.23149(59)	2.91658(70)
Fat3	−0.05126(53)	−0.01907(54)	−0.00659(54)	0.01146(55)	0.06658(59)	0.30555(70)

TABLE VII. Numerical values for the scale aq^* used to evaluate α_s in the V-scheme when computing the one-loop contributions. Note that the unsmeared results [$\mathcal{O}(p^4)$ and $\mathcal{O}(p^6)$] are mean-field improved given the formulas in Appendix B and the mean field parameter in Table I. The smeared results (fat3) are not mean-field improved. The aq^* are determined as described in Sec. II C.

am_b	7.0	4.0	3.4	2.8	1.9	1.1
$aq^*(\tilde{c}_1^{(1)})$						
$\mathcal{O}(p^4)$	2.4882(13)	2.17692(51)	2.06963(46)	1.93677(66)	1.6893(15)	1.56045(59)
$\mathcal{O}(p^6)$	2.6799(12)	2.22771(80)	2.10459(93)	1.9845(15)	1.7394(23)	2.978(11)
Fat3	2.459(22)	2.083(20)	1.961(21)	1.737(27)	2.056(14)	1.7764(19)
$aq^*(c_5^{(1)})$						
$\mathcal{O}(p^4)$	2.651(56)	2.585(30)	2.571(26)	2.560(22)	2.570(16)	2.510(15)
$\mathcal{O}(p^6)$	1.922(21)	2.035(30)	2.310(22)	2.651(34)	2.9942(87)	0.625(19)
Fat3	2.034(28)	1.937(16)	1.902(14)	1.854(12)	1.744(12)	1.92(21)
$aq^*(Z_m^{(1)})$						
$\mathcal{O}(p^4)$	1.375(35)	1.169(11)	1.0532(88)	1.1508(62)	1.1920(35)	1.0931(36)
$\mathcal{O}(p^6)$	1.370(21)	1.170(12)	0.9945(86)	1.1342(61)	1.3047(34)	1.7829(25)
Fat3	0.9598(80)	1.0007(35)	1.0416(29)	1.0784(23)	1.1316(24)	1.2024(25)
$aq^*(W_0)$						
$\mathcal{O}(p^4)$	1.0833(30)	1.0370(32)	1.0163(33)	0.9874(34)	0.9378(38)	1.3173(47)
$\mathcal{O}(p^6)$	1.0752(30)	1.0248(32)	1.0014(33)	0.9636(35)	0.9169(37)	1.4451(84)
Fat3	1.0118(27)	1.0264(27)	1.0337(27)	1.0449(27)	1.0761(27)	1.1309(28)
$aq^*(\delta C)$						
$\mathcal{O}(p^4)$	1.4998(91)	1.527(91)	1.589(74)	1.63(12)	2.508(45)	2.56(11)
$\mathcal{O}(p^6)$	1.5868(48)	1.63(12)	1.69(11)	1.79(11)	2.428(21)	2.3549(29)
Fat3	1.866(26)	1.390(76)	0.7903(92)	2.89(34)	1.699(49)	1.470(18)

TABLE VIII. Numerical values of the one-loop radiative shift relevant for non-perturbative calculations. Note that the unsmeared results ($\mathcal{O}(p^4)$ and $\mathcal{O}(p^6)$) are mean-field improved given the formulas in Appendix B and the mean field parameter in Table I. The smeared results (Fat3) are not mean-field improved. This data is plotted in Fig. 6. To determine the physical scale, q^*, we use $a^{-1} = 1.3$, 1.6, 2.2 and 3.3 GeV corresponding to very coarse, coarse, fine and superfine MILC ensembles used by the HPQCD collaboration [3]. The am_b values of 3.4, 2.8, 1.9 and 1.1 are the appropriate ones (approximately) for the b quark on very coarse, coarse, fine and superfine ensembles respectively. However, here we give results for all 4 lattice masses at each lattice spacing for completeness.

$\alpha_s(q^*)\tilde{c}_1^{(1)}$								
am_b	3.4	2.8	1.9	1.1	3.4	2.8	1.9	1.1
Very Coarse					Coarse			
$\mathcal{O}(p^4)$	0.2138(39)	0.1983(38)	0.1713(37)	0.1094(26)	0.1905(29)	0.1756(28)	0.1494(27)	0.0944(18)
$\mathcal{O}(p^6)$	0.1719(31)	0.1704(32)	0.1445(31)	−0.4417(64)	0.1533(23)	0.1513(24)	0.1265(22)	−0.4031(52)
Fat3	0.0682(16)	0.0391(12)	−0.0682(14)	−0.4775(99)	0.0605(13)	0.03424(97)	−0.0607(11)	−0.4190(73)
Fine					Superfine			
$\mathcal{O}(p^4)$	0.1641(21)	0.1503(20)	0.1260(18)	0.0788(12)	0.1403(15)	0.1278(14)	0.1059(12)	0.06573(79)
$\mathcal{O}(p^6)$	0.1323(17)	0.1298(17)	0.1071(15)	−0.3564(40)	0.1132(12)	0.1106(12)	0.0902(10)	−0.3117(31)
Fat3	0.05184(97)	0.02897(75)	−0.05227(80)	−0.3555(50)	0.04413(75)	0.02441(59)	−0.04466(60)	−0.3001(34)

TABLE IX. The same as in Table VIII but for $\alpha_s c_5^{(1)}$.

$\alpha_s(q^*)c_5^{(1)}$								
am_b	3.4	2.8	1.9	1.1	3.4	2.8	1.9	1.1
Very Coarse					Coarse			
$\mathcal{O}(p^4)$	0.1596(31)	0.1549(28)	0.1415(24)	0.0912(15)	0.1444(25)	0.1402(23)	0.1281(20)	0.0824(13)
$\mathcal{O}(p^6)$	0.04513(79)	0.05182(85)	0.0754(11)	–	0.04055(62)	0.04698(68)	0.06879(86)	–
Fat3	0.1491(34)	0.1377(31)	0.0990(23)	−0.0434(40)	0.1318(26)	0.1214(24)	0.0867(18)	−0.0384(32)
Fine					Superfine			
$\mathcal{O}(p^4)$	0.1265(20)	0.1228(18)	0.1122(15)	0.07210(95)	0.1098(16)	0.1065(14)	0.0973(11)	0.06244(72)
$\mathcal{O}(p^6)$	0.03526(45)	0.04125(51)	0.06085(66)	–	0.03037(33)	0.03584(38)	0.05324(49)	0.0915(39)
Fat3	0.1126(19)	0.1035(17)	0.0734(13)	−0.0328(25)	0.0956(15)	0.0877(13)	0.06187(92)	−0.0279(20)

[1] C. Patrignani *et al.* (Particle Data Group), Chin. Phys. C **40**, 100001 (2016).
[2] N. Brambilla *et al.*, Eur. Phys. J. C **71**, 1534 (2011).
[3] R. J. Dowdall *et al.* (HPQCD Collaboration), Phys. Rev. D **85**, 054509 (2012).
[4] J. O. Daldrop, C. T. H. Davies, and R. J. Dowdall (HPQCD Collaboration), Phys. Rev. Lett. **108**, 102003 (2012).
[5] R. J. Dowdall, C. T. H. Davies, T. C. Hammant, and R. R. Horgan (HPQCD Collaboration), Phys. Rev. D **86**, 094510 (2012).
[6] R. J. Dowdall, C. T. H. Davies, R. R. Horgan, C. J. Monahan, and J. Shigemitsu (HPQCD Collaboration), Phys. Rev. Lett. **110**, 222003 (2013).
[7] B. Colquhoun, R. J. Dowdall, C. T. H. Davies, K. Hornbostel, and G. P. Lepage (HPQCD Collaboration), Phys. Rev. D **91**, 074514 (2015).
[8] C. Hughes, R. J. Dowdall, C. T. H. Davies, R. R. Horgan, G. von Hippel, and M. Wingate (HPQCD Collaboration), Phys. Rev. D **92**, 094501 (2015).
[9] R. J. Dowdall, C. T. H. Davies, T. Hammant, and R. R. Horgan (HPQCD Collaboration), Phys. Rev. D **89**, 031502 (2014).
[10] R. J. Dowdall, C. T. H. Davies, T. Hammant, R. R. Horgan, and C. Hughes, Phys. Rev. D **92**, 039904 (2015).
[11] C. Hughes, E. Eichten, and C. T. H. Davies, Phys. Rev. D **97**, 054505 (2018).
[12] G. P. Lepage and P. B. Mackenzie, Phys. Rev. D **48**, 2250 (1993).
[13] D. Toussaint and K. Orginos (MILC Collaboration), Nucl. Phys. B, Proc. Suppl. **73**, 909 (1999).
[14] K. Hornbostel, G. P. Lepage, and C. Morningstar, Phys. Rev. D **67**, 034023 (2003).
[15] E. Follana, Q. Mason, C. Davies, K. Hornbostel, G. P. Lepage, J. Shigemitsu, H. Trottier, and K. Wong (HPQCD and UKQCD Collaborations), Phys. Rev. D **75**, 054502 (2007).
[16] A. Bazavov *et al.* (MILC Collaboration), Phys. Rev. D **93**, 094510 (2016).

[17] C. McNeile, C. T. H. Davies, E. Follana, K. Hornbostel, and G. P. Lepage (HPQCD Collaboration), Phys. Rev. D **86**, 074503 (2012).
[18] G. P. Lepage, L. Magnea, C. Nakhleh, U. Magnea, and K. Hornbostel, Phys. Rev. D **46**, 4052 (1992).
[19] C. Hughes, C. T. H. Davies, and C. J. Monahan, Phys. Rev. D **97**, 054509 (2018).
[20] C. J. Morningstar, Phys. Rev. D **50**, 5902 (1994).
[21] R. R. Horgan *et al.*, Phys. Rev. D **80**, 074505 (2009).
[22] T. C. Hammant, A. G. Hart, G. M. von Hippel, R. R. Horgan, and C. J. Monahan (HPQCD Collaboration), Phys. Rev. D **88**, 014505 (2013).
[23] M. A. Nobes, H. D. Trottier, G. P. Lepage, and Q. Mason, Nucl. Phys. B, Proc. Suppl. **106**, 838 (2002).
[24] E. Dalgic, J. Shigemitsu, and M. Wingate, Phys. Rev. D **69**, 074501 (2004).
[25] J. A. Bailey *et al.* (Fermilab Lattice and MILC Collaborations), Phys. Rev. D **92**, 014024 (2015).
[26] A. Hart, G. von Hippel, R. Horgan, and E. Müller, Comput. Phys. Commun. **180**, 2698 (2009).
[27] K. Orginos, D. Toussaint, and R. L. Sugar (MILC Collaboration), Phys. Rev. D **60**, 054503 (1999).
[28] S. J. Brodsky, G. P. Lepage, and P. B. Mackenzie, Phys. Rev. D **28**, 228 (1983).
[29] M. Lüscher and P. Weisz, Nucl. Phys. **B266**, 309 (1986).
[30] A. Hart, G. von Hippel, R. Horgan, and L. Storoni, J. Comput. Phys. **209**, 340 (2005).
[31] A. Hart, R. R. Horgan, and L. C. Storoni, Phys. Rev. D **70**, 034501 (2004).
[32] G. M. von Hippel, Comput. Phys. Commun. **181**, 705 (2010).
[33] G. P. Lepage, Lsqfit and Corrfitter Python code for Bayesian fitting, https://github.com/gplepage/corrfitter.
[34] C. McNeile, C. T. H. Davies, E. Follana, K. Hornbostel, and G. P. Lepage (HPQCD Collaboration), Phys. Rev. D **82**, 034512 (2010).
[35] G. Lepage, B. Clark, C. T. H. Davies, K. Hornbostel, P. B. Mackenzie, C. Morningstar, and H. Trottier, Nucl. Phys. B, Proc. Suppl. **106**, 12 (2002).
[36] K. Hornbostel, G. P. Lepage, C. T. H. Davies, R. J. Dowdall, H. Na, and J. Shigemitsu (HPQCD Collaboration), Phys. Rev. D **85**, 031504 (2012).
[37] K. G. Chetyrkin, B. A. Kniehl, and M. Steinhauser, Nucl. Phys. **B510**, 61 (1998).
[38] Y. Schröder, Phys. Lett. B **447**, 321 (1999).
[39] B. Chakraborty, C. T. H. Davies, B. Galloway, P. Knecht, J. Koponen, G. C. Donald, R. J. Dowdall, G. P. Lepage, and C. McNeile (HPQCD Collaboration), Phys. Rev. D **91**, 054508 (2015).
[40] E. H. Müller, Heavy-to-light decays on the lattice, Ph.D. thesis, University of Edinburgh, 2009.
[41] R. Lewis and R. M. Woloshyn, Phys. Rev. D **84**, 094501 (2011).
[42] S. Meinel, Phys. Rev. D **82**, 114502 (2010).
[43] A. J. Lee, C. J. Monahan, R. R. Horgan, C. T. H. Davies, R. J. Dowdall, and J. Koponen (HPQCD Collaboration), Phys. Rev. D **87**, 074018 (2013).
[44] D. C. Moore and G. T. Fleming, Phys. Rev. D **73**, 014504 (2006).
[45] C. E. Thomas, R. G. Edwards, and J. J. Dudek (HadSpec Collaboration), Phys. Rev. D **85**, 014507 (2012).
[46] A. Bazavov *et al.* (MILC Collaboration), Phys. Rev. D **82**, 074501 (2010).
[47] A. Hart, G. M. von Hippel, and R. R. Horgan (HPQCD Collaboration), Phys. Rev. D **79**, 074008 (2009).
[48] J. J. Dudek, R. G. Edwards, and D. G. Richards (HadSpec Collaboration), Phys. Rev. D **73**, 074507 (2006).
[49] C. M. Bouchard, G. P. Lepage, C. Monahan, H. Na, and J. Shigemitsu (HPQCD Collaboration), Phys. Rev. D **90**, 054506 (2014).